Analysis of Black Hole Reflection Spectra with Generalized Corona Geometries

Master's Thesis in Physics

Presented by

Jacob Rose

November 25, 2021

Astronomisches Institut Dr. Karl Remeis-Sternwarte

Friedrich-Alexander-Universität Erlangen-Nürnberg

Supervisor: Prof. Dr. Jörn Wilms

Abstract

Many observations of black hole X-ray spectra indicate features of broad emission lines. These features are a result of relativistic reflection of highly energetic X-ray photons in the innermost regions of the accretion disk. The effect of general relativity is at its strongest in this region and have discernible effects on the shape of atomic emission lines. The broadening of the iron line at 6.54 keV, in particular, can be used as a diagnostic tool to extract physical parameters of the black hole, e.g. the spin. The `relxill` code, with its associated model flavors was designed for this purpose. However, in order to make more accurate spin measurements, it is necessary to constrain more precisely the geometry of the irradiating source. Additionally, X-ray measurements made of the highly variable supermassive black hole Markarian 335 (Mrk 335) indicate that the X-ray spectrum is best described by a primary source with radial extension that contracts in periods of low flux and expands in periods of high flux. For this purpose, I introduce two new models, `rellineExt` and `rellxillExt`, which model the line profiles and reflected spectra resulting from an emissivity created by a ring-shaped source that rotates around the rotational axis of the black hole, respectively.

In this work I first present the necessary theory for solving the equations of motion for photons in the Kerr space-time. With these, I briefly describe the functioning of the `relxill` code, and then discuss the geometric considerations and relevant quantities for the calculation of the emissivity assuming a lamp post model. In an analogous fashion I discuss the relevant calculations necessary for the determination of the ring source emissivity. This emissivity is subsequently integrated into the `relxill` kernel, creating the `rellineExt` and `rellxillExt` models. The resulting line profiles from the ring source emissivity are shown, as well as reflected spectra. It is then shown that, in the appropriate limit, the ring source model replicates the behavior of the lamp post model and exhibits the same parameter sensitivities for this limited case, however, there still remain relevant discrepancies between the new ring source and lamp post models in the limit where they should coincide. The effect of the new ring radius parameter, d, was then analyzed and compared to the lamp post model. The models are then used to analyze 2014 *NuSTAR* observations of Mrk 335. The preliminary results are in rough agreement with previous observations. However, there appear signs of systemic issues in the calculation of the reflected spectra. Furthermore, certain results indicate that the determination of specific parameters may contribute to the observed discrepancies. Further work on alleviating these issues is necessary. However, despite these issues, the newly implemented ring source constrains the primary source in a manner that appears to agree with previous emissivity profile calculations and indicates the viability of this approach.

Zusammenfassung

Viele Röntgenbeobachtungen von Schwarzer Löcher weisen breite Emissionsslinien auf. Diese entstehen durch relativistische Reflektion von hochenergetischen Röntgenphotonen in den innersten Regionen der Akkretionsscheibe. Die Effekt, beschrieben durch die Allgemeine Relativitätstheorie, sind in dieser Region am stärksten und haben erkennbare Auswirkungen auf die Form der atomaren Emissionslinien. Insbesondere die Verbreitung der Eisenlinie bei 6,54 keV kann verwendet werden, um physikalische Parameter des Schwarzen Lochs, wie beispielsweise den Drehimpuls, zu bestimmen. Der Code relxill wurde zu diesen Zweck entwickelt. Um genauere Spinmessungen durchzuführen ist es jedoch notwendig, die Geometrie der Strahlungsquelle besser einzuschränken. Zusätzlich deuten Beobachtungen des hochvariablen supermassiven Schwarzen Lochs Markarian 335 darauf hin, dass das Röntgenspektrum am besten durch eine Primärquelle mit radialer Ausdehnung beschrieben werden kann. Bei niedrigem Fluss zieht sich diese Primärquelle zusammen, und dehnt sich bei hohem Fluss aus. Um Beobachtungen dieser Art zu modellieren, führe ich zwei neue Modelle ein, `rellineExt` und `rellxillExt`, die die Linienprofile und die reflektierten Spektren berechnen. Diese Spektren resultieren aus einem Emissionsprofil, das von der rotierenden, ringförmigen Quelle erzeugt wird. In dieser Arbeit stelle ich zunächst die notwendige Theorie zur Lösung der Bewegungsgleichungen für Photonen in der Kerr-Raumzeit vor. Anhand dieser Gleichungen beschreibe ich die Funktionsprinzip des `rellxill` Codes und erörtere die geometrischen Überlegungen und relevanten Größen für die Berechnung des Emissionsprofils unter der Annahme, dass sich die Quelle auf der Rotationsachse des Schwarzen Loches befindet (Lamp-Post Modell). In gleicher Weise erörtere ich dann die relevanten Berechnungen, die für die Bestimmung des Emissionsgrades der Ringquelle erforderlich sind. Die neuen Modelle `rellineExt` und `rellxillExt` implementieren dieses Emissionsprofil. Die sich daraus ergebenden Linienprofile werden ebenso gezeigt wie die reflektierten Spektren. Es wird gezeigt, dass das Ringquellenmodell asymptotisch das Verhalten des Lamp-Post Modells nachbildet und für diesen begrenzten Fall dieselben Eigenschaften aufweist. Es bestehen jedoch noch immer Diskrepanzen zwischen dem neuen Ringquellen- und dem Lamp-Post-Modell in der Grenze, in der sie übereinstimmen sollten. Anschließend wird die Auswirkung des neuen Ringradiusparameters, d, analysiert und mit dem Lamp-Post Modell verglichen. Die Modelle werden dann verwendet, um eine NuSTAR Beobachtungen von Markarian 335 zu analysieren. Die vorläufigen Ergebnisse stehen in grober Übereinstimmung mit früheren Beobachtungen. Es gibt jedoch Anzeichen für systemische Abweichungen bei der Berechnung der reflektierten Spektren. Weiterhin kann die Bestimmung bestimmter Parameter zu den beobachteten Diskrepanzen beitragen. Deshalb sind weitere Arbeiten zur Behebung dieser Probleme notwendig. Trotz dieser Probleme schränkt die neu implementierte Ringquelle die primäre Quelle in einer Weise ein, die mit früheren

Berechnungen des Emissionsprofils übereinstimmt und somit die generelle Machbarkeit dieses Ansatzes zeigt.

Contents

Contents

1 Introduction

1.1 Introduction to black holes

Black holes have been a source of intrigue and mystery for physicists since the derivation of the Schwarzschild solution (1916) to the Einstein Field Equations (Einstein 1916). Due to the many strange physical paradoxes created by black holes, their existence was initially rejected at large by the scientific community. However, with the discovery of Cygnus X-1 (Clark et al. 1968) and the failure of other sufficient models to explain the data, particularly the radial velocity (Webster & Murdin 1972), the existence of the first detected black hole was gradually accepted. The Schwarzschild solution describes the gravitational field resulting from a point particle. The main consequence of this solution is that there exists a region around the central point where the effect of gravity is sufficiently strong such that light itself cannot even escape. This boundary is known as the "event horizon." The relation between the radius at which this event horizon occurs is given as

$$r_S = \frac{2GM}{c^2}, \tag{1.1}$$

where M is the mass of the black hole, c is the speed of light, and G is the Newtonian gravitational constant. In theory, any body of matter could become a black hole, if packed sufficiently dense enough. The earth, for example, if packed inside an spherical volume with a radius of approximately 9.8 mm, would become a black hole. Due to the intense forces required to compress matter densely enough, however, the physical avenues for their formation are rather limited and, as a result, there are two general categories. Galactic black holes (GBHs) are formed at the end of a star's life after the resulting supernova and usually contain a few solar masses (Mirabel 2017). These are usually found in binary systems i.e., they orbit a neighboring star. The black hole is able to feed itself using the mass of the nearby star which slowly gathers around the black hole. The resulting radiation, having an appreciable luminosity in the X-ray spectrum (Shakura & Sunyaev 1973), can be detected by telescopes on satellites and their spectra can be analyzed. In addition both types of black holes can be detected due to "gravitational lensing", which is an effect caused by the bending of light around the massive object.

The second class of black holes are known as super-massive black holes (SMBHs). As the name suggest these are generally quite massive, typically containing millions or billions of solar masses. The quasar TON 618 was estimated to contain a black hole of nearly 66 billion solar masses (Shemmer et al. 2004), making it one of the largest black holes ever observed. All of the known SMBHs are found at the center of galaxies. A

subset of these black holes are known as active galactic nuclei (AGN) and are notable for their very bright appearance. Compared to other SMBHs, these typically are quite bright over the entire electromagnetic spectrum, from radio waves to intense gamma rays. Unfortunately the formation of SMBHs are not as well understood as their smaller counterparts. A linear hierarchy of black holes ranging in size from smaller to GBH to SMBHs is not likely to exist (Richards et al. 2006). SMBHs are either believed to have formed as a result of various runaway processes (Rees 1984), or gravitational potentials of clumps of dark matter, which originated from density fluctuations as a result of the Big Bang, act as a catalyst for the formation of SMBHs (Ferrarese & Merritt 2000).

Most observable black holes contain an accretion disk, which is the result of matter congregating around the black hole. There exist a variety of models for these disks with the most basic being the standard alpha disk (Shakura & Sunyaev 1973), which presents a model based on hydrodynamics lacking magnetic fields. In this model, the accreting matter spirals around the black hole in a disk which is geometrically thin but optically thick. The particles that compose this disk all have their own angular momenta and corresponding angular velocities. In the course of their orbit they undergo turbulent flow, interacting with and bouncing off other particles in the disc, reducing their overall momentum and angular velocity around the black hole. Taking magneto-hydrodynamics into account, it can be shown that this turbulence and the shear forces caused by small magnetic fields can create an effective viscosity, which transports the deprived angular momentum outwards. The lost angular momentum of the particle causes it to fall into a orbits closer to the black hole and thereby gaining kinetic energy from the converted gravitational potential (Balbus & Hawley 1991). The increased speed causes frictional heating and as a result the innermost region of the accretion disk has the highest temperatures, which can reach up to 10^8K (Shakura & Sunyaev 1973). As a result of these high temperatures it is believed that the matter flow in this region consists mainly of plasma, which would explains the disk's optical thickness/opacity (Shakura & Sunyaev 1973).

Although GBHs and SMBHs differ greatly in size, they share many properties in common. The same solutions to Einstein's equations describe both small and large black holes alike and both can be described by the parameters mass, spin and electric charge (Carter 1971). Thus black holes are also some of the simplest objects in physics. Because the universe is electromagnetically neutral the charge is can be neglected. This leaves us with just two parameters, the spin a and mass M, which describe black holes in their entirety. The spin parameter in particular, $a = J/M$, is related to the angular momentum J of the black hole and can theoretically range from -1 to 1. However it was shown that due to the interaction of photons from the accretion disk a more practical limit is $|a_{\mathrm{max}}| = 0.998$ (Thorne 1974), where negative values indicate the retrograde spinning of the black hole with respect to the accretion disk.

2

1.2 Spectroscopy

The field of X-ray astronomy is younger than its visible light and radio wave counterparts. Unlike those sources of electromagnetic radiation, X-rays are effectively blocked from reaching the surface by the earth's atmosphere. Gamma rays, UV, and infrared radiation suffer from this problem as well, as is illustrated in Fig. 1.1. In order to effectively measure X-rays emitted by black hole systems, it is necessary to get detectors above the earth's atmosphere. This was initially done in a variety of ways the first being in 1948 when American researchers utilizing confiscated V-2 rockets made the first solar X-ray measurements. Rockets were in continued use, leading to first discovery of an X-ray source outside the solar system, Scorpius X-1. The first X-ray measurements of AGNs were taken such satellite-attached detectors aboard the Aerobee rocket in 1965, which provided evidence for Cygnus A and M87 (Byram et al. 1966).
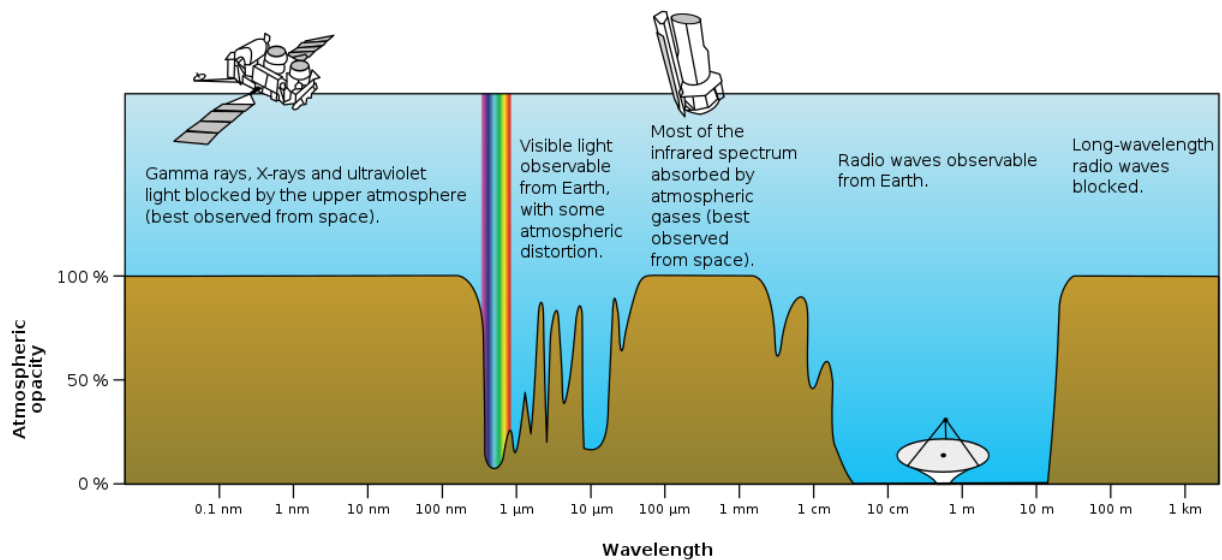

Figure 1.1: Plot of Earth's atmospheric opacity to various wavelengths of electromagnetic radiation. Credit: NASA

In order to understand these measured spectra, it is necessary to understand have a basic understanding of spectroscopy. A brief introduction of these concepts are given here. According to the classical theory of electromagnetism, charged particles under an acceleration emit radiation. The photons emitted by such freely moving charged particles give rise to a continuous spectrum of energies. There are, however, many processes involved in the creation of the continuous spectral component, however an important one for AGNs is inverse Compton scattering, which will be discussed in the next section. However, quantum mechanics tells us that electrons within a bound potential (e.g. in an atom) are limited to discrete states as illustrated for hydrogen in Fig. 1.2.
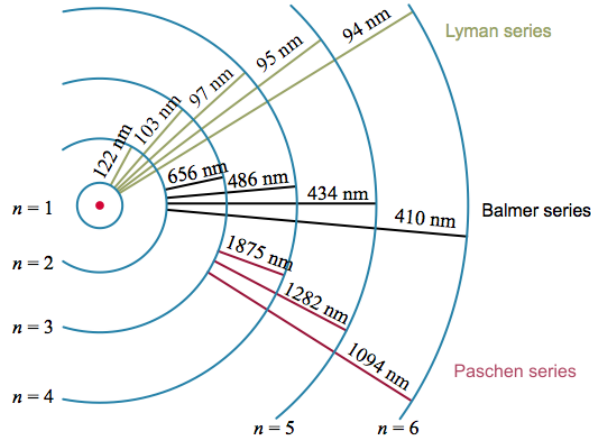
Figure 1.2: A diagram showing the principal energy levels of hydrogen and corresponding wavelength of the emitted radiation. Credit: math-science-resources.com

The orbiting electrons can be excited into higher states by incoming photons where it absorbs the photon containing exactly the energy difference between the two states. These causes dips in the detected spectra, known as absorption lines. When these excited electrons return back to their original states, they will emit radiation corresponding to the energy difference of those two states, which can be seen as a sharp peak in the spectrum, referred to as an emission line. Normally these lines are quite narrow, corresponding to the need for a precise photon energy to cause the transition but in the context of AGNs and black holes more generally, the emitted radiation undergoes severe gravitational distortion causing these lines to broaden, which is discussed in more detail in Section 1.3. As a quick nomenclatural side-note, the innermost atomic shell, which is associated with the quantum number $n = 1$ is known as the K-Shell, followed by L, and M, for $n = 2$ and $n = 3$ etc. We denote ionization states with Roman numerals, where I denotes the neutral state, II is once ionized and the pattern continues. They can also be labeled by the number of electrons contained, for example one electron would be called "hydrogen-like," and "helium-like" with two. The electron number is what determines which transitions are possible so this choice of naming convention is quite appropriate. These peaks and dips allow us to determine
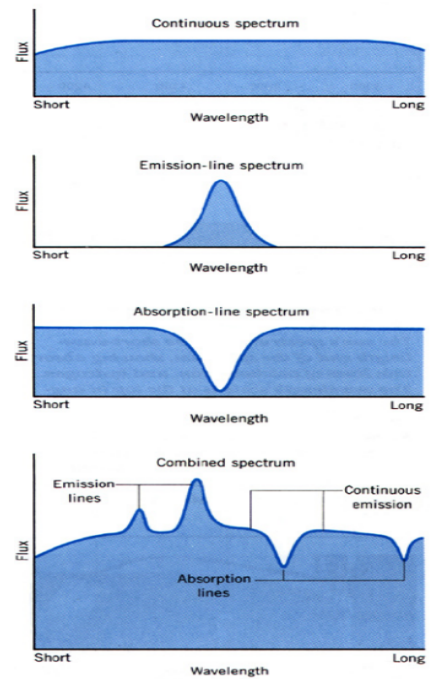

Figure 1.3: Example emission and absorption lines. Credit: Dr. Travis A. Rector & Dr. Andrew W. Puckett

the chemical composition of many astrophysical bodies, due to each element having its own unique emission and absorption spectrum, a theoretical example being shown in Fig. 1.3.

1.3 The X-ray Spectrum

Because black holes do not emit radiation of their own, the measured spectra is a result of the accretion disk. It is believed that low-energy photons are inverse Compton scattered by relativistic electrons near the black hole above the accretion disc (Haardt & Maraschi 1991) with a cut-off for high energy photons due to the limited distribution of the relativistic electrons. Due to disk's temperature decreasing as $r^{-3/4}$ (Shakura &
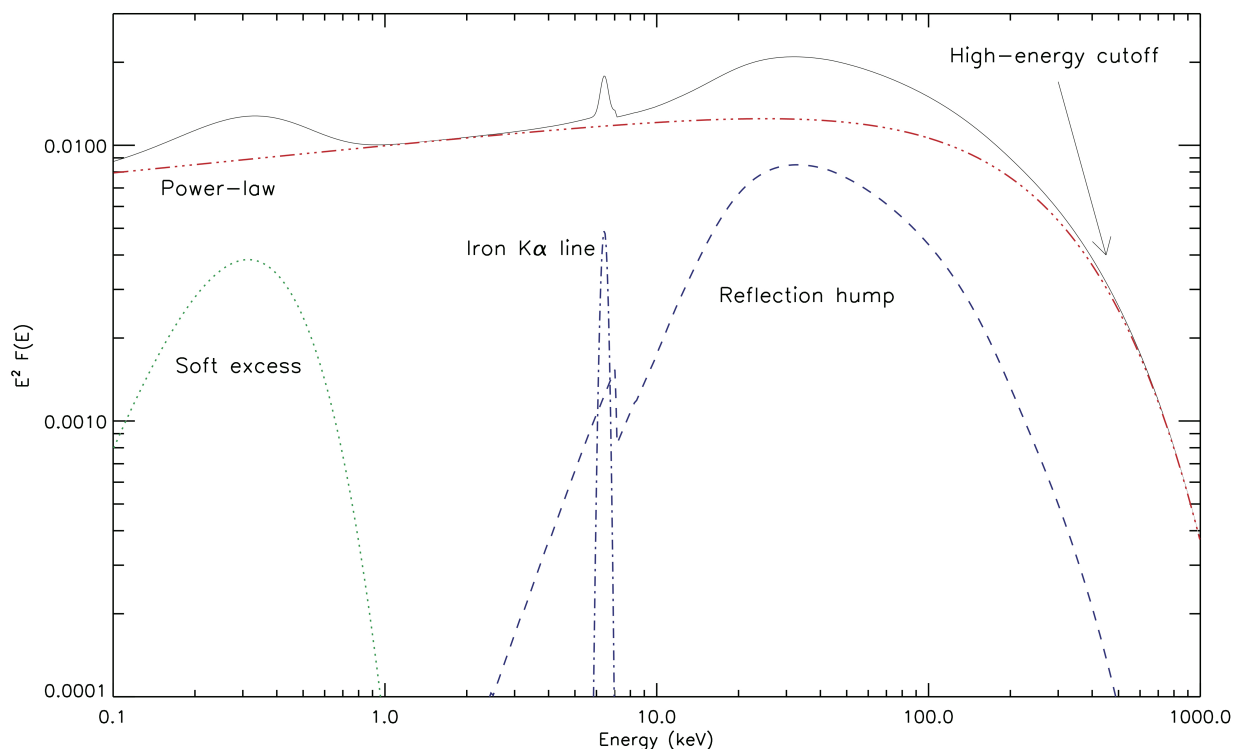
Figure 1.4: Typical 0.1-1000 keV spectrum of an unabsorbed AGN. Credit: Ricci et al. 2011, PhD thesis

Sunyaev 1973), the spectrum is a stretched black body spectrum. The observed spectra show a significant component in the high energy region. The up-scattered photons also re-illuminate the accretion disc resulting in an additional reflected spectral component resulting in a "reflection hump" as is illustrated in Fig. 1.4. This reflected radiation makes up a large contribution to the overall spectrum and is modeled by the XILLVER model (García et al. 2013). Of particular note is the emission line at approximately 6.4 keV, which is due to the Kα transition in iron, which is relatively abundant in the accretion

disk. This reflected radiation is heavily distorted due to its close vicinity of the black hole and this effect is modeled by `relxill` (Dauser 2010) which this thesis makes significant use of. The degree and shape of this distortion allows us to determine properties of the black hole, such as the spin (Dauser et al. 2016) (need better reference here). The presence of this reflection hump indicates and the resulting relativistic distortion suggests the existence of a hard X-ray source near the black hole. The initial assumption was that there was a hot corona near the inner accretion disk. Assuming the intensity of this corona is proportional to the disk emissivity (Shakura & Sunyaev 1973)

$$I(r) \propto \frac{1}{r^3} \left(1 - \sqrt{\frac{r_{\mathrm{in}}}{r}}\right), \tag{1.2}$$

with r_{in} being the inner radius of the accretion disc, we can see for large values of r, the spectrum is proportional to r^{-3} and will flatten towards the inner edge of the disk. However, the introduction of high signal-to-noise ratio data from satellites such as *XMM-Newton* showed a disagreement with this assumption. In various observations, it was shown that the data was explained quite well by emissivities which are substantially steeper in the inner regions of the disk (Wilms et al. 2001; Brenneman et al. 2011; Gallo et al. 2011). Furthermore, it would stand to reason that there would be a positive correlation between the reflected flux and the continuum flux. A higher continuum
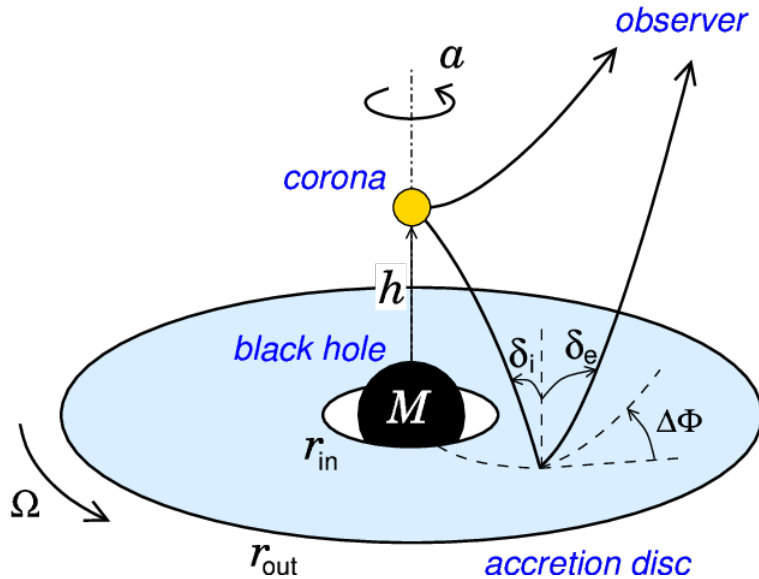
Figure 1.5: A sketch of the lamp-post model. The corona is modeled as a point source at height h along the rotational axis of the black hole. The radiation that hits the disk does so at the inclination given by δ_i and is re-emitted at an angle of δ_e. Credit: (Caballero-Garcia et al. 2016)

flux corresponds to higher disk emissivity, which in turn would ultimately lead to more up-scattered radiation being reflected by the disk. Unfortunately, observations of MCG-6-30-15 (Fabian & Vaughan 2003; Miniutti et al. 2003) showed large variation in the

continuum flux while the reflected component stayed relatively constant. Instead of a standard corona, in what is also known as the "Lamp Post" model, a primary source which is found along the rotation axis of the black hole at a given height, h, can explain the detail quite well (Martocchia et al. 2002; Vaughan & Fabian 2004) and this model is illustrated in Fig 1.5. The steeper emissivity in the inner regions can be explained by the concentration of the radiation into the inner regions of the disk, due to light-bending and energy shift, which will be described in detail in Chapter 3. In addition, the observed relation between the continuum flux and the reflected flux are succinctly explained. The increased concentration of inner radii photons result in a higher reflected component and less photons for the continuum (Miniutti & Fabian 2004). Increasing the height decreases the inner photon concentration, meaning more photons can escape, thereby adding to the continuum flux.

1.4 Thesis Aim

There are a number of tools for the calculation of spectra of irradiated accretion disks from Jet-Base corona (Dauser et al. 2013; García et al. 2013; Fukumura et al. 2009) and even tools to simulate the emissivities of extended sources (Wilkins & Fabian 2012). The former cannot, however, model sources which are not located along the rotational axis and the latter suffer from long run times, due to their reliance on Monte Carlo simulations to compute spectra. This thesis attempts to present a new `relxill`-based model of a ring shaped primary source as an extended version of the existing `relxill` lamp-post model (`relxill_lp`), which can be utilized in comparison and fitting to measured spectral data from X-ray satellites such as *XMM-Newton* and *NuSTAR*. Much of the ray-tracing simulations for the creation of the necessary data tables were done by Licklederer (2019), which we will discuss here as well. However this thesis integrates this data to create a new usable model as part of `relxill` for use in X-ray analysis software such as `XSPEC` (Arnaud 1996) or `ISIS` (Houck & Denicola 2000) for direct comparison with measured data, and attempts to use it to analyze data from the AGN, Mrk 335.

A introduction to the necessary theory governing motion around black holes will be covered in Chapter 2 as well as very brief discussion on the ray-tracing simulations. Chapter 3 will focus on the `relxill` code, the computation of the relativistic line (relline) profile, and the computation of the full `relxill` model as well as with the general ring shaped source. In Chapter 4 we analyze first the relline profiles and then the full `relxill` spectra of the ring source and compare them to the simpler lamp post model. A detailed analysis of the fitting results to Mrk 335 will be given in Chapter 5 as well as a comparison to lamp post fitting for the same source. Finally, in Chapter 6 we give a conclusion and outlook for potential further research.

2 Black Hole Theory

Shortly after the publishing of Einsteins Field Equations, Karl Schwarzschild presented his solutions assuming spherical symmetry, known as the Schwarzschild metric. This gives rise to a region around the spherical center where neither massive or massless particles cannot escape typically referred to as the event horizon, and anything contained within that is know well known as the so called "black hole." However the Schwarzschild solution is not unique in its ability to describe black holes. The Kerr solution (Kerr 1963) solution also shares this trait, with the assumption that the black hole spins on a rotational axis.

As the Kerr metric serves as the mathematical basis for nearly all of the work in this thesis and related work, a short treatment of the related equations and relevant properties for this thesis will be discussed in this chapter. The formalism here follows the most closely the work of Chandrasekhar (1983) and heavily draws from the introduction to black hole theory given by (Licklederer 2019). For those well versed in the formalism of general relativity and black hole physics, some following sections may be skipped without much consequence, however one might still find it instructive so that the precise mathematical notation is understood as it can vary from reference to reference. All formula here are given in natural units (i.e. $G \equiv c \equiv 1$).

2.1 The Kerr Metric

There exists no general solution to the Einstein field equations. However, by assuming certain symmetries, one can derive particular exact solutions. In the Schwarzschild metric, one assumes a static, spherically symmetric vacuum. However for the Kerr metric, we relax the assumption on spherical symmetry and instead only require that the metric be axially symmetric and static. This generalization is quite necessary as during stellar collapse and black hole formation, angular momentum is conserved and leads to the existence of black holes with non-vanishing angular momentum.

Starting with the metric tensor g, in its most general form, we apply the symmetry conditions for using a suitable chart. The requirement of the previously mentioned symmetry conditions of a stationary and axis-symmetric spacetime translate to the existence of a time-like Killing vector ξ, and space-like Killing vector X, with space-like, closed orbits, respectively. In addition we also require that both symmetries ensure compatibility with the condition that the Lie-derivative $\mathcal{L}_\xi X = 0$. In contrast to the Schwarschild metric, we require only that the metric tensor in a coordinate system is invariant under simultaneous inversion of the t and ϕ coordinates, i.e. $(t, \phi, x^1, x^2) \to (-t, -\phi, x^1, x^2)$. As a result we see that $g_{02} \to -g_{02}$, $g_{03} \to -g_{03}$, and $g_{12} \to -g_{12}$,

$g_{13} \to -g_{13}$ implying that they must vanish. This leaves us with

$$ds^2 = g_{00}dt^2 + 2g_{01}d\phi dt + g_{11}d\phi^2 + [g_{22}(dx^2)^2 + 2g_{23}dx^2 dx^3 + g_{33}(dx^3)^2]. \qquad (2.1)$$

The term in the square brackets can can be brought into a "diagonal" form (**?**) (change reference):

$$ds^2 = -e^{2\nu}(dt)^2 + e^{2\psi}(d\phi - \omega dt)^2 + e^{2\mu_2}(d\tilde{x}^2)^2 + e^{2\mu_3}(d\tilde{x}^3)^2 \qquad (2.2)$$

where ν, ψ, μ_2, and μ_3 are functions of the coordinates $\tilde{x}^2, \tilde{x}^3$, and μ_2 and μ_3 are free to be restrained by a coordinate choice. The only other information required at this point is the use of the vacuum Einstein field equations, that is

$$R_{ab} - \frac{1}{2}g_{ab}R = G_{ab} = 0 \qquad (2.3)$$

and a practical choice of coordinate on μ_2 and μ_3. Because it is not that instructive to work through full derivation and simplification of the resulting equations from the vacuum field equations, it is sufficient to regard the choice of coordinate condition forced on μ_2 and μ_3.

The particular gauge choice presented here implies no loss of generality (Chandrasekhar 1983), however is strongly motivated by physical considerations. The polar angle θ with respect to the axis of symmetry is chosen as $\tilde{x}^3$ and the radial coordinate r as $\tilde{x}^3$. The metric we seek should emit an event horizon i.e. a smooth null-surface. Following Licklederer (2019), a general 2-dimensional null-surface can be given by

$$N(x^1, x^2) = 0 \qquad (2.4)$$

and the null condition being

$$g^{ab}(\partial_a N)(\partial_b N) = 0 \qquad\qquad a, b = 1, 2 \qquad (2.5)$$

for a smooth function N. The null condition means that the normal vectors of the surface at every point are null. The vectors, η, that are tangent to the null-surface obey the condition $g^{ab}\eta_a \partial_b N = 0$ by definition. Therefore $\partial_a N$ itself is a tangent vector, i.e. $\partial_a N = g_{ab}\frac{d\gamma^b(t)}{dt}$ for a curve γ that lies inside the null-surface. Thus at every point of the surface, there exists a tangent vector η for which $\eta^a \eta_a = 0$. Geometrically the null-surface at every point is tangent to the light cone at that point. As a result, the light cone is entirely on one side of the null-surface and is at that point tangent to it. The smoothness of the function N and as well as the metric tensor field g also show that all the light cones along the null-surface lie on the same side. The future-direction world line of a massive or massless particle can only cross the null-surface in one direction. The null-surface then forms an event horizon as characterized earlier in this chapter. Note that for the sake of generality, a 2-dimensional null-surface was considered.

Because of the aforementioned axis-symmetry of the coordinate ϕ and stationarity, the function that describes the surface of the event horizon depends solely on r and θ (Licklederer 2019), thus

$$N(r, \theta) = 0, \qquad (2.6)$$

for a smooth function N and the tangent space of the surface is spanned by ∂_t and ∂_ϕ. Taking the condition that the surface be null (Eq. 2.5) and the standard form for the axis-symmetric (Eq. 2.2), stationary spacetime, we have

$$e^{2(\mu_3-\mu_2)}(\partial_r N)^2 + (\partial_\theta N)^2 = 0. \qquad (2.7)$$

Using our special gauge choice let

$$e^{2(\mu_3-\mu_2)} = \Delta(r), \qquad (2.8)$$

where $\Delta(r)$ is simply some function of r. From Eq. 2.7, it follows that the equation for the null-surface is given by

$$\Delta(r) = 0. \qquad (2.9)$$

Using the latter condition, that the surface be spanned by ∂_t and ∂_ϕ, necessitates that the determinant of the subspace (t, ϕ) vanish on the surface. Thus,

$$e^{2\psi+2\nu} = 0. \qquad (2.10)$$

Since we did not specify $\Delta(r)$ previously, let us assume

$$e^{\psi+\nu} = \Delta^{1/2}f(\theta), \qquad (2.11)$$

allowing us to separate the parts dependent on r, and θ, for some $f(\theta)$ which is regular on the entire null-surface. Making use of parts of the vacuum field equations

$$R_{11} + R_{00} \equiv 0 + 0 = 0, \qquad (2.12)$$

and Eqs. 2.8 and 2.11 as well as the regularity of $f(\theta)$ and the convexity of the event horizon, it then follows

$$\frac{\partial^2}{\partial r^2}\Delta = 2 \qquad\qquad\qquad f(\theta) = \sin\theta. \qquad (2.13)$$

This allows us to write $\Delta(r)$ as

$$\Delta(r) = r^2 - 2Mr + a^2, \qquad (2.14)$$

where M and a are simply constants of integration, however when investigating limits of the Kerr solution, they acquire the physical meaning of mass and angular momentum per unit mass of the black hole, respectively. With this particular choice, we have

$$e^{\mu_3-\mu_2} = \Delta(r)^{1/2} \qquad\qquad e^{\psi+\nu} = \Delta(r)^{1/2}\sin\theta. \qquad (2.15)$$

This completes the derivation of the Kerr solution and the end result can be expressed by the following line element, given in Boyer-Lindquist (Boyer & Lindquist 1967) coordinates as

$$ds^2 = -\Sigma\frac{\Delta}{\rho^2}(dt)^2 + \frac{\rho^2}{\Sigma}\left(d\phi - \frac{2aMr}{\rho^2}dt\right)^2\sin^2\theta + \frac{\Sigma}{\Delta}(dr)^2 + \Sigma(d\theta)^2, \qquad (2.16)$$

where

$$\Sigma = r^2 + a^2 \cos^2 \theta \tag{2.17}$$

$$\Delta = r^2 - 2Mr + a^2 \tag{2.18}$$

$$\rho^2 = (r^2 + a^2)^2 - a^2 \Delta \sin^2 \theta. \tag{2.19}$$

We can return from Boyer-Lindquist coordinates back to Cartesian coordinates (see Carroll (2004)) by

$$x = \sqrt{r^2 + a^2} \sin \theta \cos \phi \tag{2.20}$$

$$y = \sqrt{r^2 + a^2} \sin \theta \sin \phi \tag{2.21}$$

$$z = r \cos \theta \tag{2.22}$$

The functions $e^{2\nu}$, $e^{2\psi}$, $e^{2\mu_2}$, and $e^{2\mu_3}$ from Eq. 2.2, can then be identified by comparing the coefficients of the Kerr metric, giving

$$e^{2\nu} = \frac{\Sigma \Delta}{\rho^2} \tag{2.23}$$

$$e^{2\psi} = \frac{\rho^2 \sin^2 \theta}{\Sigma} \tag{2.24}$$

$$e^{2\mu_2} = \frac{\Sigma}{\Delta} \tag{2.25}$$

$$e^{2\mu_3} = \Sigma \tag{2.26}$$

$$\omega = \frac{2aMr}{\rho^2}. \tag{2.27}$$

As previously mentioned, taking the limits of the Kerr metric we can understand the meaning of the constants M, and a. By taking $r \to \infty$, the Kerr metric approaches the Scharzschild solution

$$ds^2_{\text{Schwarzschild}} = -\left(1 - \frac{2M}{r}\right) dt^2 + \frac{1}{1 - \frac{2M}{r}} dr^2 + r^2(d\theta^2 + \sin^2 \theta d\phi^2). \tag{2.28}$$

We can identify M as the mass of the black hole. If we take the limit as $a \to 0$ we also retrieve the Schwarzschild solution. As the Schwarzschild solution describes a non-rotating body, we can deduce that a is related to the angular momentum, and investigating the Kerr metric we can physically interpret it as the angular momentum per unit rest mass of the black hole. The Kerr metric gives rise to various physical phenomena, such as frame-dragging first described by Lense-Thirring precession (Lense & Thirring 1918), which has been confirmed by experiments like the Gravity Probe B (Everitt et al. 2011).

The condition $\Delta(r) = 0$ can be evaluated as this causes a coordinate singularity according to 2.16, from which we can determine the event horizon,

$$r_{\pm} = 1 \pm \sqrt{1 - a^2}. \tag{2.29}$$

This gives us two event horizons, where the outer horizon r_+ determines the size of the black hole. The inner horizon is a Cauchy horizon, a region in which the existence of close time-like curves can exist (Licklederer 2019).

2.2 Equations of Motion

In order to calculate the paths that particles take it is necessary to calculate the geodesic, which can be thought of as the "straightest" path through curved spacetime. Following Licklederer (2019), we can find geodesics by minimizing the action

$$S_{(g;\gamma]} = \frac{1}{2} \int d\lambda \; g_{\gamma(\lambda)}(\gamma(\lambda), \dot{\gamma}(\lambda)) \tag{2.30}$$

where γ is the curve through spacetime. Finding the functional minimum of this action we can derive the geodesic equation.

$$\frac{d^2 x^a}{d\lambda^2} - \Gamma^a_{bc} \frac{dx^b}{d\lambda} \frac{dx^c}{d\lambda} = 0 \tag{2.31}$$

where $x(\lambda)$ is the representation of $\gamma(\lambda)$ in any chart (U, x) and Γ^a_{bc}. Due to the stationary nature of the Kerr metric, there exists a time-like Killing vector ξ, and its axial symmetry corresponds to the existence of a Killing vector X with space-like, closed orbits. As solutions to the Killing equation

$$\nabla_{(a} Y_{b)} = 0, \tag{2.32}$$

where ∇ is a covariant derivative and the brackets indicate symmetrization of the indices. It follows that along a geodesic, $\gamma = \mathrm{x}^{-1} \circ x$, the quantity

$$Y_a \frac{dx^a}{d\lambda} = \text{const}, \quad \text{where } Y \in \{\xi, X\} \tag{2.33}$$

is conserved. To demonstrate this we can take its change along the geodesic

$$\frac{d}{d\lambda} \left(Y_a \frac{dx^a}{d\lambda} \right) = \frac{dx}{d\lambda} \nabla_a \left(Y_b \frac{dx^b}{d\lambda} \right). \tag{2.34}$$

Expanding this out, we have

$$\frac{dx^a}{d\lambda} Y_b \nabla_a \left(\frac{dx^b}{d\lambda} \right) + \frac{dx^a}{d\lambda} \frac{dx^b}{d\lambda} \nabla_a (Y_b) = 0. \tag{2.35}$$

We know the first term is zero due to the geodesic equation, and second term is zero due to the Killing condition. Thereby confirming the conservation of $Y_a \frac{dx^a}{d\lambda}$. The resulting conservation of these quantities for ξ and X correspond to the energy E and angular momentum l, respectively. The rest mass is also conserved, however this is not a result of a spacetime symmetry. The conservation of the rest mass corresponds to having a constant valued Hamiltonian. The Hamiltonian can also be derived from the action and has the following form

$$H = \frac{1}{2\Sigma} \left(\Delta p_r^2 + p_\theta^2 - \frac{\rho^2}{\Delta} p_t^2 + \left(\frac{1}{\sin^2 \theta} - \frac{a^2}{\Delta} \right) p_\phi^2 - \frac{4aMr}{\Delta} p_t p_\phi \right), \tag{2.36}$$

where

$$p_t = -\left(1 - \frac{2Mr}{\Sigma}\right)\dot{t} - 2Mar\frac{\sin^2\theta}{\Sigma}\dot{\phi} \tag{2.37}$$

$$p_r = \frac{\Sigma}{\Delta}\dot{r} \tag{2.38}$$

$$p_\theta = \Sigma\dot{\theta} \tag{2.39}$$

$$p_\phi = -\left(r^2 + a^2 + a\frac{\rho^2}{\Sigma}\omega\sin^2\theta\right)\sin^2\theta\dot{\phi} - \frac{\rho^2}{\Sigma}\omega\sin^2\theta\dot{t}. \tag{2.40}$$

The Hamiltonian does not depend on neither ϕ nor t , as these give rise to related conserved quantities, which we can identify as the angular momentum, $p_\phi = l$, and the energy, $-p_t = E$, confirming the conservation quantities from the Killing condition. We can make use of Hamiltonian-Jacobi formalism to obtain a further conserved quantity known as the Carter (1968) constant and defined as

$$Q = p_\theta^2 + \cos^2\theta\left[a^2(\mu^2 - p_t^2) + \frac{p_\phi^2}{\sin^2\theta}\right], \tag{2.41}$$

with $\mu = 1$ for massive particles and $\mu = 0$ for massless particles. This is not a standard symmetry but arises from a separation ansatz in the Hamiltonian-Jacobi formalism for θ and r. Due to the four conserved quantities the geodesic is uniquely determined and thus we are able to solve for it. The equations which describe photon trajectories (Bardeen et al. 1972) (in natural units $G = M = c = 1$) are given by

$$\Sigma\frac{dt}{d\sigma} = -a(aE\sin^2\theta - \lambda) + (r^2 + a^2)\frac{T}{\Delta} \tag{2.42}$$

$$\Sigma\frac{dr}{d\sigma} = \pm\sqrt{V_r} \tag{2.43}$$

$$\Sigma\frac{dt}{d\sigma} = \pm\sqrt{V_\theta} \tag{2.44}$$

$$\Sigma\frac{dt}{d\sigma} = -a\left(a - \frac{\lambda}{\sin^2\theta}\right) + a\frac{T}{\Delta} \tag{2.45}$$

where σ is an affine parameter or the "proper time" for a massless particle, where

$$V_r = r^4 - (q + \lambda^2 - a^2)r^2 + 2\left[q + (\lambda - a)^2\right]r - a^2q \tag{2.46}$$

$$V_\theta = r^4 - q^2 + a^2\cos^2\theta - \lambda^2\cot^2\theta \tag{2.47}$$

$$T = r^2 + a^2 - \lambda a \tag{2.48}$$

$$\lambda = \frac{l}{E} \tag{2.49}$$

$$q^2 = \frac{Q}{E^2} \tag{2.50}$$

The different signs in Eqs. 2.43-2.44 are for increasing (positive) and decreasing (negative) values of r and θ. Carter was able to determine that these equations are integrable and derived their corresponding integral forms (for a massless particle) (Carter 1968) as

$$\pm \int^r \frac{dr'}{\sqrt{V_r(r')}} = \pm \int^\theta \frac{d\theta'}{\sqrt{V_\theta(\theta')}} \tag{2.51}$$

$$\sigma = \int^r \frac{r'^2}{\sqrt{V_r(r')}} dr' + a^2 \int^\theta \frac{\cos^2 \theta'}{\sqrt{V_\theta(\theta')}} d\theta' \tag{2.52}$$

$$t = \sigma + 2 \int^r \frac{r'T}{\Delta\sqrt{V_r(r')}} dr' \tag{2.53}$$

$$\phi = a \int^r \frac{T}{\Delta\sqrt{V_r(r')}} dr' + a^2 \int^\theta \frac{\lambda - a^2 \sin^2 \theta'}{\sin^2 \theta' \sqrt{V_\theta(\theta')}} d\theta'. \tag{2.54}$$

where

$$\Delta = r^2 - 2r + a^2 \tag{2.55}$$

$$V_r = (r^2 + a^2)^2 - \Delta(q^2 + a^2) \tag{2.56}$$

$$V_\theta = q^2 - \cos^2 \theta \left[\frac{\lambda^2}{\sin^2 \theta} - a^2 \right] \tag{2.57}$$

with r being the distance from and a being the spin of the black hole. The equations are given in units where $G \equiv M \equiv c \equiv 1$.

2.2.1 Lamp Post Source

For the lamp post model, we can make the assumption that $\theta = 0$. However, given the form of V_θ, this leads to difficulties as the equation diverges. This divergence is not a physical one, as there is no physical reason why the source could not be located on the rotational axis of the black hole, but a mathematical one. To avoid this divergence, one simply applies the following conditions (Licklederer 2019)

$$\lim_{\theta \to 0} \left| \frac{\lambda^2}{\sin^2 \theta} \right| < \infty \tag{2.58}$$

$$\lim_{\theta \to 0} \lambda = 0. \tag{2.59}$$

The first condition eliminates the divergence in V_θ, however a consequence is that any photon which is emitted along the axis of symmetry must have zero angular momentum. This allows for a massive simplification the equations of motion. The restriction in Eq. 2.58 allows us to simplify V_θ to

$$V_\theta(\theta) = q^2 + a^2 \cos^2 \theta, \tag{2.60}$$

for which now $\theta = 0$ is well defined, resulting in

$$V_\theta(0) = q^2 + a^2. \tag{2.61}$$

This problem can be easily understood by considering the fact that along the symmetry axis, the idea of a ϕ-direction makes no sense. If you are on the north pole, which direction is east, or west? There is only south. The situation described above is directly analogous. With this in mind, we can deduce that the initial direction of the photon trajectories which start on the rotational axis are determined by a singular angle δ. We can then determine the relation between this emission angle q (Dauser 2010)

$$\sin \delta = \frac{(p_h)_a (n_h^{(\theta)})^a}{(p_h)_b (u_h)^b} = \frac{\sqrt{\frac{V_\theta}{\Sigma}}|_{\theta=0}}{-u_h^t} = \frac{\sqrt{h^2 - 2h + a^2}}{h^2 + a^2} \sqrt{q^2 + a^2}, \tag{2.62}$$

where $n_h^{(\theta)}$ is the normal vector in the θ-direction. We can find the single non-zero component of the particle four-velocity, u_h^t, which can be determined from the normalization condition

$$1 \overset{!}{=} u_a u^a = (u_h^t)^2 g_{tt}(h) = -(u_h^t)^2 \frac{\Delta(h)}{h^2 + a^2}. \tag{2.63}$$

From this we can determine the expression for q,

$$q = \sin^2 \delta \sqrt{\frac{h^2 - 2h + a^2}{h^2 + a^2}}. \tag{2.64}$$

Finally with the constants of motion q and λ, we can specifically determine the photon momentum

$$p_a = E\left(-1, \pm\frac{V_r}{\Delta}, \pm\sqrt{V_\theta}, \lambda\right), \tag{2.65}$$

and now we are able to solve the equations of motion numerically.

2.2.2 General Source

Having determined the relevant equations of motion for the lamp post model, I determine, following very closely the work of (Licklederer 2019), the relevant equations of motion for a general source. For a more general model, and the ring source which is presented in this thesis, it is efficient to choose a chart in which the equations of motion are simplest and locally non-rotating observers will provide these charts. If the initial conditions are specified in another reference frame, it is possible to change to a locally non-rotating observer with a general Lorentz transformation. Following Licklederer (2019) (and by extension Bardeen et al. (1972)), we construct the locally non-rotating frame (LNRF) by the basis vectors

$$e_{(a)}(\text{LNRF}) = e_{(a)}^\nu \partial_\nu \tag{2.66}$$

where

$$e_{(a)}^\nu = \begin{pmatrix} e^{-\nu} & 0 & 0 & \omega e^{-\nu} \\ 0 & e^{-\mu_2} & 0 & 0 \\ 0 & 0 & e^{-\mu_3} & 0 \\ 0 & 0 & 0 & e^{-\psi} \end{pmatrix} \tag{2.67}$$

which constitute a frame with the property

$$e^i_{(a)}e_{(b)i} = \eta_{(a)(b)} \tag{2.68}$$

and ω indicates the rotational velocity of the LNRF with respect to the coordinate frame. If expressed in terms of the initial momenta with respect to the LNRF, the equations of motion will take a simple form. Using the Hamiltonian Eq. 2.36, Eq. 2.40 and Eqs. 2.42-2.45 we can express the four-momentum of a photon in Boyer-Lindquist coord. as

$$p_\mu = E\left(-1, \text{sign}(r)\frac{\sqrt{V_r}}{\Delta}, \text{sign}(\theta)\sqrt{V_\theta}, \lambda\right). \tag{2.69}$$

Because they are the components of a co-vector, they can be easily transformed into components in the LNRF by

$$\bar{p}_{(a)} = e^\mu_{(a)}p_\mu, \tag{2.70}$$

where $\bar{p}_{(a)}$ are the components of the four-momentum in the LNRF. Following Shakura (1987) we have

$$\bar{p}_{(t)} = -Ee^{-\nu}(1 - \lambda\omega) \tag{2.71}$$

$$\bar{p}_{(r)} = \text{sign}(r)Ee^{-\mu_2}\frac{\sqrt{V_r}}{\Delta} \tag{2.72}$$

$$\bar{p}_{(\theta)} = \text{sign}(\theta)Ee^{-\mu_3}\sqrt{V_\theta} \tag{2.73}$$

$$\bar{p}_{(\phi)} = E\lambda e^\psi. \tag{2.74}$$

From Eqs. 2.71 and 2.71 we can calulate λ:

$$\lambda = \frac{\sin\theta\frac{\bar{p}_{(\phi)}}{\bar{p}_{(t)}}}{-\Sigma\frac{\sqrt{\Delta}}{\rho^2} + \omega\sin\theta\frac{\bar{p}_{(\phi)}}{\bar{p}_{(t)}}}, \tag{2.75}$$

and Eq. 2.71 gives us

$$E = -\frac{\bar{p}_{(t)}e^\nu}{(1 - \lambda\omega)}. \tag{2.76}$$

Although it is possible to calculate these quantities from components of the four-momentum $\bar{p}(a)$ with respect to the LNRF, it may be the case that the components are given with respect to another frame. It is then possible to a general Lorentz transformation to obtain the desired LNRF components. Considering a reference frame with physical velocities v_r, v_θ and v_ϕ with respect to the LNRF. One can obtain the LNRF components via $\bar{p}_{(a)} = \alpha^{(b)}_a p'_{(b)}$ where p' and $\alpha^{(b)}_a$ is the Lorentz matrix (Misner 1973) given as

$$\alpha^{(b)}_a = \begin{pmatrix} \gamma & -\gamma v_r & -\gamma v_\theta & -\gamma v_\phi \\ -\gamma v_r & 1 + \frac{\gamma^2 v_r^2}{1+\gamma} & \frac{\gamma^2 v_r v_\theta}{1+\gamma} & \frac{\gamma^2 v_r v_\phi}{(1+\gamma)} \\ -\gamma v_\theta & \frac{\gamma^2 v_r v_\theta}{(1+\gamma)} & 1 + \frac{\gamma^2 v_\theta^2}{(1+\gamma)} & \frac{\gamma^2 v_\theta v_\phi}{(1+\gamma)} \\ -\gamma v_\phi & \frac{\gamma^2 v_r v_\phi}{(1+\gamma)} & \frac{\gamma^2 v_\theta v_\phi}{(1+\gamma^2} & 1 + \frac{\gamma^2 v_\phi^2}{(1+\gamma)} \end{pmatrix}. \tag{2.77}$$

2.3 The Accretion Disk

A good understanding of the accretion disc is needed for the following chapters and we describe the model here. We assume a geometrically thin accretion disc on a stable orbit in the equatorial plane which gives us

$$\dot{\theta} = 0 \qquad \text{and} \qquad \theta = \frac{\pi}{2}. \qquad (2.78)$$

From Eqs. 2.41 and 2.50, we can see under these assumptions that $Q = q = 0$. The disk is most easily modeled by a continuum of particles each on circular orbits with varying radii. For these orbits the following is necessary that

$$\ddot{r} = 0, \qquad \dot{r} = 0 \qquad \text{and} \qquad r = \text{const}, \qquad (2.79)$$

which leads to

$$\frac{dV_r}{dr} = 0 \qquad \text{and} \qquad V_r = 0. \qquad (2.80)$$

It is then possible to solve for E and L (Bardeen et al. 1972) which are given:

$$\frac{E}{\mu} = \frac{r\sqrt{r} - 2M\sqrt{r} + a\sqrt{M}}{r^{3/4}\sqrt{r\sqrt{r} - 3M\sqrt{r} + 2a\sqrt{M}}} \qquad (2.81)$$

$$\frac{L}{\mu} = \frac{\sqrt{M}(r^2 - 2a\sqrt{Mr} + a^2)}{r^{3/4}\sqrt{r\sqrt{r} - 3M\sqrt{r} + 2a\sqrt{M}}} \qquad (2.82)$$

Using these, we can calculate the angular velocity of the disk:

$$\Omega = \frac{d\phi}{dt} = \frac{\sqrt{M}}{r\sqrt{r} + a\sqrt{M}} \qquad (2.83)$$

This applies to both pro- and retrograde orbits with respect to the spin of the black hole itself i.e. $a > 0$ and $a < 0$. In keeping with Bardeen et al. (1972), the stable orbits on the orbiting disk imposes

$$\frac{d^2V_r}{dr} \leq 0 \qquad (2.84)$$

and solving for the resulting system of equations reveals that only certain radii $r \geq r_{\text{ms}}$ where

$$r_{\text{ms}} = M\left(3 + Z_2 - \text{sign}(a)\sqrt{(3 - Z_1)(3 + Z_1 + 2Z_2)}\right) \qquad (2.85)$$

$$Z_1 = 1(1 - a^2)^{\frac{1}{3}}\left[(1 + a)^{\frac{1}{3}} + (1 - a)^{\frac{1}{3}}\right] \qquad (2.86)$$

$$Z_2 = \sqrt{3a^2 + Z_1^2}. \qquad (2.87)$$

If we evaluate Eq. 2.85 for maximally, non-rotating, and maximally counter-rotating disks we obtain $r_{\text{ms}} = 1.24\ r_g$ for $a = 0.998$, $r_{\text{ms}} = 6\ r_g$ for $a = 0$, and $r_{\text{ms}} = 8.994\ r_g$ for $a = -0.998$. If we assume that the inner radius of the accretion disk is the r_{ms}, then we can see that for black holes in which the spin and disk rotation are aligned, the accretion disk reaches much closer to the black hole. This effect is critically relevant in understanding the concentration of photons in the inner region of the disk.

2.4 Ray Tracing

In order to generate the necessary tables for integration in the model for the relxill code ray-tracing simulations were necessary. This work was done by Licklederer (2019) using the publicly available YNOGK-code created by Yang & Wang (2013), adapted for this purpose. Using Weierstrass and Jacobi elliptical functions, it is possible to express all coordinates and affine parameters as analytical and numerical functions of a parameter p, which is simply an integral value along the geodesic. This improves on earlier work done by Dexter & Agol (2009), the main differences being the faster computational times and no longer needing to specific the "turning points" in advance.

The general approach to solving the equations of motion is to express the coordinates (t, ϕ, r, θ) by an affine parameter p. The equations of motions are then expressed as equations of the constants of motion as well as the affine as well as the parameter p. These new equations can then be brought into a standard form which can be evaluated using Carlson's method (Carlson 1989, 1991, 1992, 1995). Then what remains is to determine the constants of motion from the initial conditions, which can be done by providing expressions of λ and q in terms of the affine parameter p. In the end, finding the incident radius of an emitted photon on the disk becomes simply a problem of root finding. More details into the exact inner workings of the code can be found in both Licklederer (2019) and Yang & Wang (2013).

3 Modeling Relativistic Reflection

Among the various models available for modeling X-ray spectra of black holes, such as `kerrdisk` (Brenneman et al. 2011) or `reflionx` (Ross & Fabian 2005), this thesis makes use of and expands upon `relxill` (Dauser 2014). `relxill` combines the `xillver` (García et al. 2013) and `relline` (Dauser 2010) code, and features a proper angular treatment of reflected radiation (García et al. 2014) as well as the ability to constrain the reflection fraction (Dauser et al. 2014).

3.1 The Purpose of the Model

The `relxill` code is the combination of the previous `relline` (Dauser 2010) and `xillver` (García et al. 2013) codes. `xillver` calculates the reflected spectrum from an accretion disk by solving the equations of radiative transfer, energy balance, and ionization equilibrium in a Compton-thick medium. It makes use of `xstar` (Kallman 1999) routines for the calculation of the ionization structure of the photo-ionized gas, as well as using its atomic data. `relline` describes the emission lines broadened due to relativistic smearing (Dauser 2010). Unlike the simple convolution of `relconv` and `xillver`, which smears the angle-averaged reflection, `relxill` properly takes into account the relativistic effects for each region in the accretion disk. This is necessary because the angle of emission from the disk is not necessarily the same as its inclination (García et al. 2014). The emission angle changes drastically near the black hole and therefore a proper treatment of this angular variation must be taken into account. At higher inclinations differences between the angle-averaged convolution and the `relxill` model are more prevalent as demonstrated in Figure 3.1, which is due to increased relativistic effects. `relxill` also permits the direct fitting of the reflection fraction for relativistically smeared spectra (Dauser et al. 2014) and can be used to constrain the spin of the black hole. This can provide us with the opportunity to determine more accurately the precise geometry of the illuminating source.

3.2 Calculation of the Line Profile

The `relline` model (Dauser 2010) calculates an emission line which undergoes the relativistic distortion due to the black hole gravitational potential as well as the rotation of the accretion disk. While calculations of line profiles from black holes with negative spin values existed (Jaroszynski 1997), the models that existed for use in `isis` (Houck & Denicola 2000) or `xspec` (Arnaud 1996) for line profiles such as `diskline` (Fabian et al.
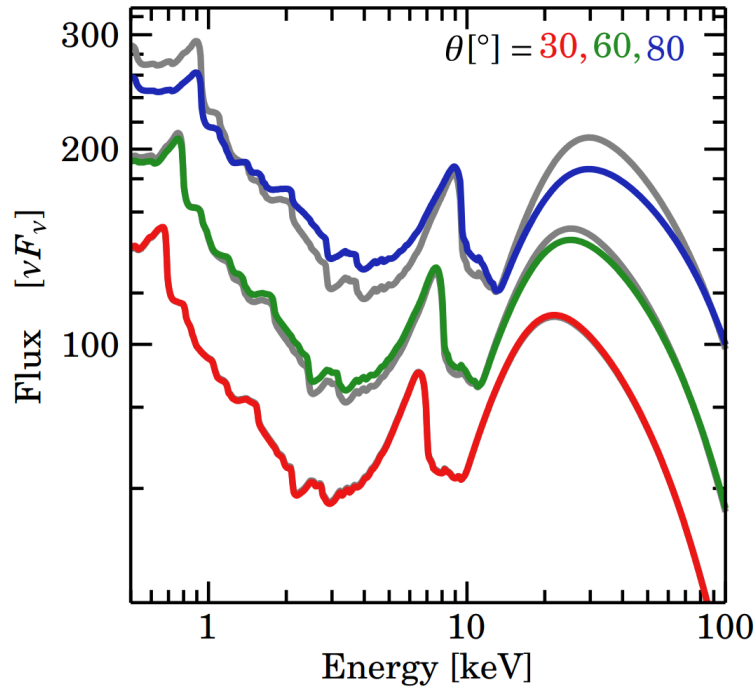
Figure 3.1: Reflected spectrum for `relxill` for varying inclination angles. In gray is the simple convolution of `relconv` on the `xillver` spectra. Credit: García et al. (2014)

1989), `laor` (Laor 1991), or `kerrdisk` (Brenneman & Reynolds 2006) did not. We give here a brief summary of the derivation of the line profile following the work of Dauser (2010).

3.2.1 Radiation Transport

Assuming an observer very far from the system, the black hole can be considered as a point source. In this case, it is necessary to integrate the local emitted emissivity, $I_{E_e}(r_e, \theta_e)$, to obtain the observed intensity $I_E^{\mathrm{obs}}(\theta_o)$. This specific intensities depends only on the radius, r_e, and the emission angle θ_e, because of the symmetry of the system. We define the intensity of photons at energy E as (Misner 1973)

$$I_E = \frac{EdN}{AdEd\Omega dt}. \tag{3.1}$$

where dN is the number of photons into the solid angle direction $d\Omega$, which flow through the area A in the time dt. This quantity is unfortunately not Lorentz invariant as it depends on the chosen frame of reference. As a result it is necessary to search for a way to convert emitted intensity I_{E_e} at the accretion disk to the measured intensity I_{E_o}. Following Misner (1973), we can show that the number density, $\mathcal{N} = \delta N/(V_x V_p)$ of photons is an invariant, with

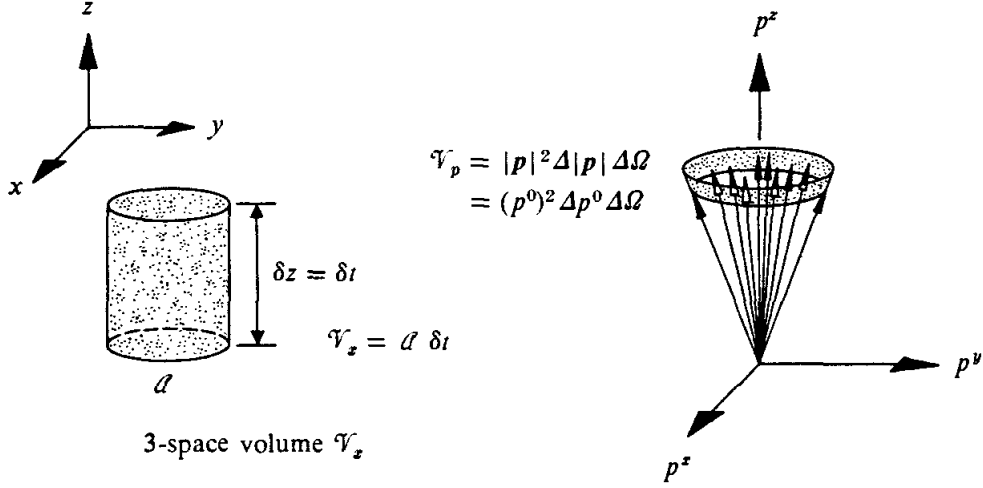$$\frac{d\mathcal{N}}{d\lambda} = 0 \tag{3.2}$$

Figure 3.2: A sketch of the volumes of the phase space $V_x V_p$ for the momentum space V_p as well as the position space V_x, needed to calculate the number density. Taken from Misner (1973).

which is the collision-less Boltzmann equation in curved space, where $V_x V_p$ is the phase space volume of N identical particles. Taking into account explicit considerations (see Fig. 3.2) leads to $V_x = Adt$ and $V_p = d\Omega E^2 dE$. We also require all particles to be the same, which from $\vec{p}^2 = m^2$ dictates that the four-momenta lie on a hyperboloid. This allows us identify the specific intensity with the number density and the result is

$$\frac{I_E}{E^3} = \mathcal{N} = \text{const.} \tag{3.3}$$

Now we are able to integrate easily over the entire accretion disk, after projecting onto a plane which is perpendicular to the line of sight. This plane is spanned by impact parameters α, and β, which are related to the solid angle (Cunningham 1975) by

$$d\alpha d\beta = r_o^2 d\Omega, \tag{3.4}$$

where r_o is the distance to the system. The observed intensity now can be expressed as

$$I_E(\theta) = \int \left(\frac{E}{E_e}\right)^3 I_{E_e}(r_e, \theta_e) \, d\alpha d\beta \ . \tag{3.5}$$

We can define the energy shift $g = E/E_e$ where E_e is the energy in the emitter's frame and E is the energy in the observer's frame. The energy shift can be calculated from the metric. Using the fact that the observer measures in flat Minkowski space, and using the expressions for the four momentum of the photon in the Kerr metric, the general expression is given as (Dauser 2010)

$$g = \frac{E}{E_e} = -\frac{E}{p_\mu^e u_\mu} = \frac{\sqrt{r_e}\sqrt{r_e^2 - 3Mr_e + 2a\sqrt{Mr_e}}}{r_e\sqrt{r_e} + a\sqrt{M} - \beta(a)\sqrt{M}\lambda}. \tag{3.6}$$

λ is dependent on the rotational direction of the black hole, and as a result changes sign in the case of negative spin, although the direction of the photon does not. To account for this we introduce

$$\beta(a) = \begin{cases} +1 & \text{for } a \geq 0 \\ -1 & \text{for } a < 0 \end{cases}. \tag{3.7}$$

This is required, as a change in direction of the rotation implicitly requires one to flip the coordinate system, but we do not want the photon to change direction. Normally this would be accounted for the by sign of a however, the case of $a = 0$ necessitates the choice of a particular coordinate system.

Knowing at which energy the photon is emitted from the disk and the resulting energy shift, we are able to calculate the energy at which we should observe it. It is, however, convenient to express the solid angle Ω in terms of the emission radius r_e and the relative redshift g^*. This relative energy energy shift is defined as

$$g^* = \frac{g - g_{\min}}{g_{\max} - g_{\min}} \in [0, 1]. \tag{3.8}$$

where $g_{\min}$ and $g_{\max}$ are the min and max energy shifts, respectively. For ease of calculation, Cunningham (1975) defined the transfer function as

$$f(g^*, r_e, \theta_o) = \frac{r_o^2}{\pi r_e} g \sqrt{g^*(1 - g^*)} \left| \frac{\partial \Omega}{\partial(g^*, r_e)} \right|. \tag{3.9}$$

In order to calculate the transfer function for given values r_e and g^*, we must calculate the Jacobian after calculating $g_{\min}$ and $g_{\max}$. Following Dauser (2010), the impact parameters α and β are related to the constants of motion λ and q by

$$\alpha = -\frac{\lambda}{\sin \theta_o} \qquad\qquad \beta = \pm \sqrt{V_\theta(\theta_o)} \tag{3.10}$$

Therefore

$$r_o^2 d\Omega = d\alpha d\beta = \left| \frac{\partial(\alpha, \beta)}{\partial(\lambda, q)} \right| d\lambda dq = \frac{q}{\sin(\theta_o)\beta} d\lambda dq \tag{3.11}$$

and the Jacobian is

$$r_0^2 \left| \frac{\partial \Omega}{\partial(g^*, r_e)} \right| = \frac{q(g_{\max} - g_{\min})}{\sin(\theta_o)\beta} \left| \frac{\partial(\lambda, q)}{\partial(g, r_e)} \right|. \tag{3.12}$$

Using this, as well as the equations above we can derive a new expression for the observed intensity

$$I_E(\theta) = \frac{1}{r_o^2} \int_{r_{\rm rms}}^{\infty} \int_0^1 \frac{\pi r_e g^2 f(g^*, r_e, \theta_o)}{\sqrt{g^*(1 - g^*)}} I_{E_e}(r_e, \theta_e) \, dg^* dr, \tag{3.13}$$

where $r_{\rm in}$ and $r_{\rm out}$ are the inner and outer radii of the accretion disc. Although we have parameterized the accretion disk in (r_e, g^*) space, it is still defined properly as this

parametrization leads to conserved quantities λ and q. A more detailed explanation of the numerical process can be found in Dauser (2010) and Speith et al. (1995) but I will give a quick summary here. To start, an initial r_e is chosen representing a ring within the accretion disk. The corresponding $g_{\min}$ and $g_{\max}$ are calculated and the ring is split into parts according to their energy shifts using Eq. 3.8. For each g^* we find the corresponding λ by rearranging Eq. 3.6, and insert them into the integral equations Eqs. 2.51 - 2.54, where q is the only undetermined quantity left, which is then solved numerically for the (g^*, r_e) values which ensure that the photons actually hit the observer. After having fully determined the equations of motion, we can calculate the derivative in Eq 3.12 and thereby determine the transfer function. As the accretion disk is composed of many concentric rings, the process is then repeated for various r_e values within the disk. All of these steps are performed using algorithms created by Speith et al. (1995) with modifications for negative spins introduced by Dauser (2010).

3.3 Analysis of the Emissivity

In order to more efficiently calculate the line profile Dauser et al. (2010) takes a Green's function approach and takes the specific intensity from the disk as mono -energetic at E_e,

$$I_E(r_e, \theta_e, E_e) = \delta(E - E_e)I_\epsilon(r_e, \theta_e), \tag{3.14}$$

where I_ϵ is the disk emissivity, the determination of which is of great importance and the topic of this section. If we insert this into Eq. 3.13 and evaluate the integral we derive

$$I_E(\theta) = \int_{r_{\mathrm{in}}}^{r_{\mathrm{out}}} \frac{\pi g^3 r_e f(g^*, r_e, \theta)}{E_e(g_{\max} - g_{\min})\sqrt{g^*(1 - g^*)}} I_\epsilon(r_e, \theta_e)dr_e \tag{3.15}$$

In order to calculate the reflected spectrum then, we must first determine the emissivity. The emissivity is key to understanding the geometry of the hard X-ray source. For a given geometry its emissivity can be calculated and, with the help of `relxill`, compared to measured X-ray spectra. Although `relxill` makes use of a simple empirical power law emissivity, $I_\epsilon \propto r_e^{-\alpha}$, `relxill_lp` makes use of the lamp post geometry. Because the ring source that I introduce in Chapter 4 resembles the lamp post model, I will, for the sake of completeness, discuss the determination of the lamp post emissivity here, concepts from which are also relevant for the ring source model.

3.3.1 Geometric effects

In the simple case of a point source located along the rotational axis, assuming no general relativistic effects, the emissivity relation (Dauser 2014) is given as

$$I_i(r, h) \propto \frac{1}{A(r_i, \Delta r_i)} = \frac{\cos \delta_i}{r_i^2 + h^2} = \frac{h}{(r_i^2 + h^2)^{3/2}}, \tag{3.16}$$

where h is the height of the source above the black hole and r is the radial distance along the accretion disc. However, due to the strong gravitational field in the vicinity

of a black hole, relativistic effects become crucial for understanding the shape of the emissivity profile. Photons that are emitted from the source in the range $[\delta, \delta + \Delta\delta]$ are distributed on a ring on the accretion disc with an area of $A(r, \Delta r)$. Following Dauser et al. (2013), the proper area of a ring at radius r with thickness Δr is given as

$$A(r, \Delta r) = 2\pi \sqrt{\frac{r^4 + a^2 r^2 + 2a^2 r}{r^2 - 2r + a^2}} \Delta r, \tag{3.17}$$

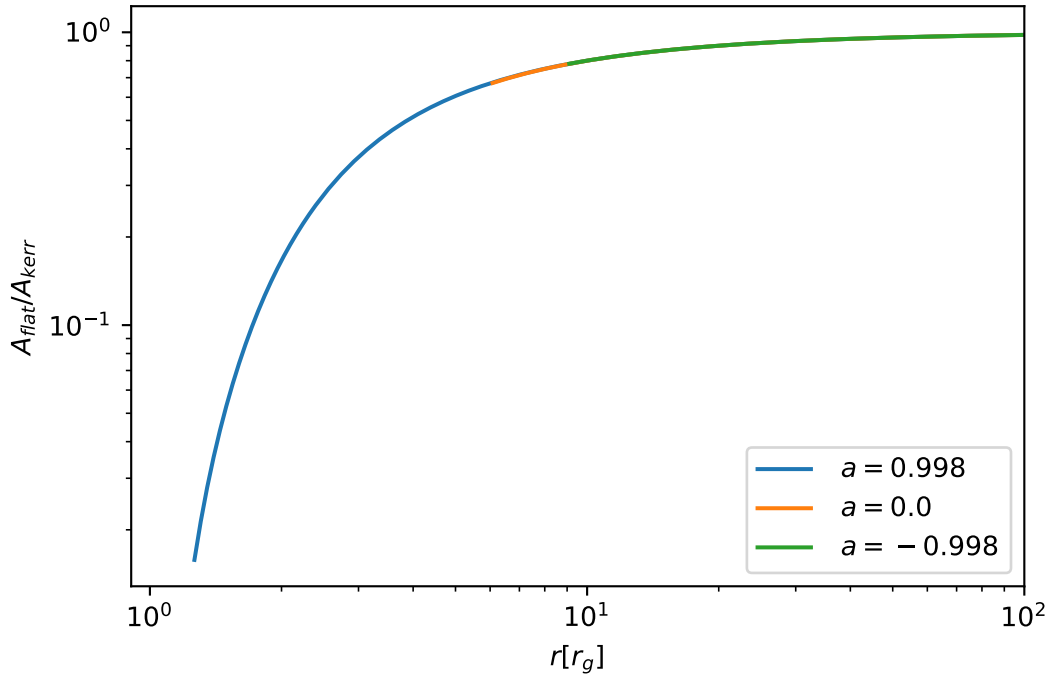in the observer's rest frame (Wilkins & Fabian 2012). To calculate the irradiation in

Figure 3.3: The impact on the proper area as a function of the radial distance from the black hole. Varied for three different spin values.

the rest frame of the disc, it is necessary to take into account its rotation at relativistic speeds. As a consequence, its area will be contracted. Taking the Keplerian velocity profile from the Kerr metric (Bardeen et al. 1972; Wilkins & Fabian 2012), we find the disc's Lorentz factor to be

$$\gamma^{(\phi)} = \frac{\sqrt{r^2 - 2r + a^2}(r^{3/2} + a)}{r^{1/4}\sqrt{r\sqrt{r} + 2a - 3\sqrt{r}}\sqrt{r^3 + a^2 r + 2a^2}}. \tag{3.18}$$

As a result we find that the incident intensity with these geometric considerations taken into account (Dauser et al. 2013) to be

$$I_i^{\text{geo}} = \frac{1}{A(r, \Delta r)\gamma^{(\phi)}}. \tag{3.19}$$

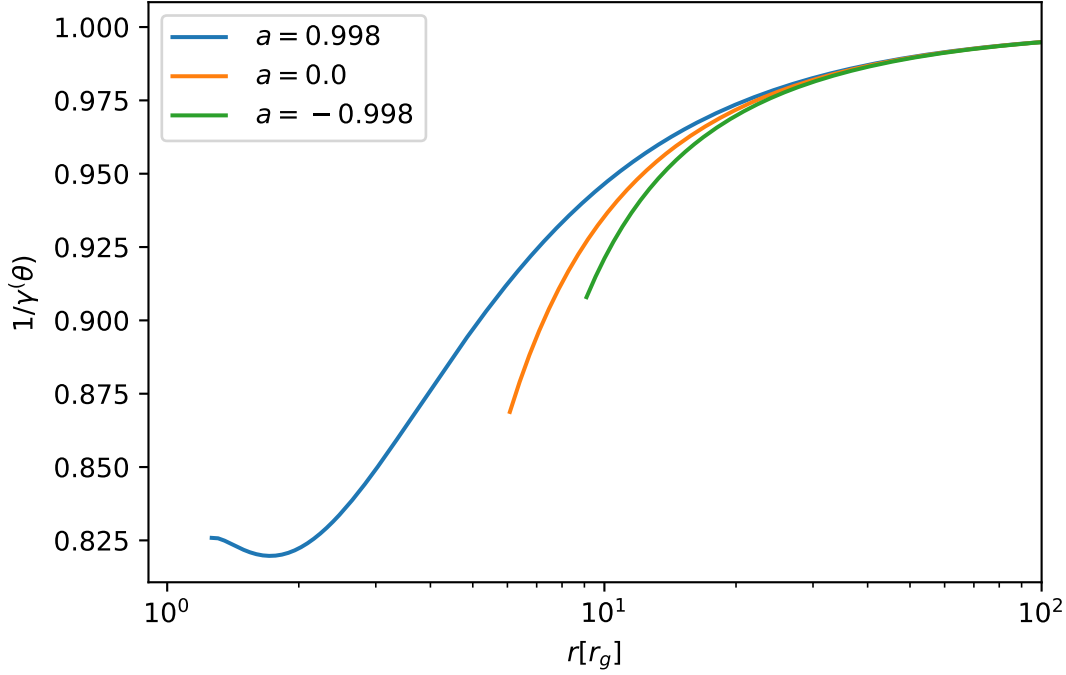Due to the relative motion of the emitting source and the accretion disc, as well as

Figure 3.4: The beaming factor as a function of the radial distance from the black hole. Varied for three different spin values.

general relativity, there will be a shift in energy of the irradiated spectrum. Following Dauser et al. (2013), we take into account the fact the number of photons is conserved we can write

$$N_e^{(\mathrm{ph})} \Delta t_e \Delta E_e = \text{const.} = N_i^{(\mathrm{ph})} \Delta t_i \Delta E_i. \tag{3.20}$$

where $N_e^{(\mathrm{ph})}$ ($N_i^{(\mathrm{ph})}$) is flux of emitted (incident) photons. If a power-law shape is assumed for the emitted radiation

$$N_e^{(\mathrm{ph})} = E_e^{-\Gamma} \tag{3.21}$$

where Γ is the photon index, then the photon flux on the accretion disc can be determined by

$$N_i^{(\mathrm{ph})}(r,a) = E_i^{-\Gamma} g_{\mathrm{lp}}(r,a)^{\Gamma}, \tag{3.22}$$

due to $\Delta E_e / \Delta E_t = 1/g_{\mathrm{lp}}$ and $\Delta t_e / \Delta t_i = g_{\mathrm{lp}}$. The flux incident on the accretion disc is dependent on where the photon makes contact, r, and using this the incident flux can be calculated as

$$I_\epsilon(r,h) = I_i^{\mathrm{geo}} g^{\Gamma} = \frac{g^{\Gamma}}{A(r,\Delta r)\gamma^{(\phi)}}. \tag{3.23}$$

From Figs. 3.3 - 3.4 it is easy to see that the geometric effects are largest in magnitude at the innermost radii. The spin of the black hole is an especially relevant parameter

because it determines the radius of marginal stability and it is assumed in the `relxill` kernel, by default, that the accretion disk extends down to this radius. For large radii the differences between the spins as well as the relativistic effects gradually disappear. This makes sense as one would expect given that at larger distances the Kerr metric gradually approximates to the Schwarzschild metric.

3.3.2 Energy Shift

Lastly we must determine the energy shift from the source to the disk in order to be able to calculate the emissivity. The energy shift is dependent on the chosen geometry of the source. Here we will analyze the result for the lamp-post model and will discuss the energy shift for the ring source in Chapter 4.
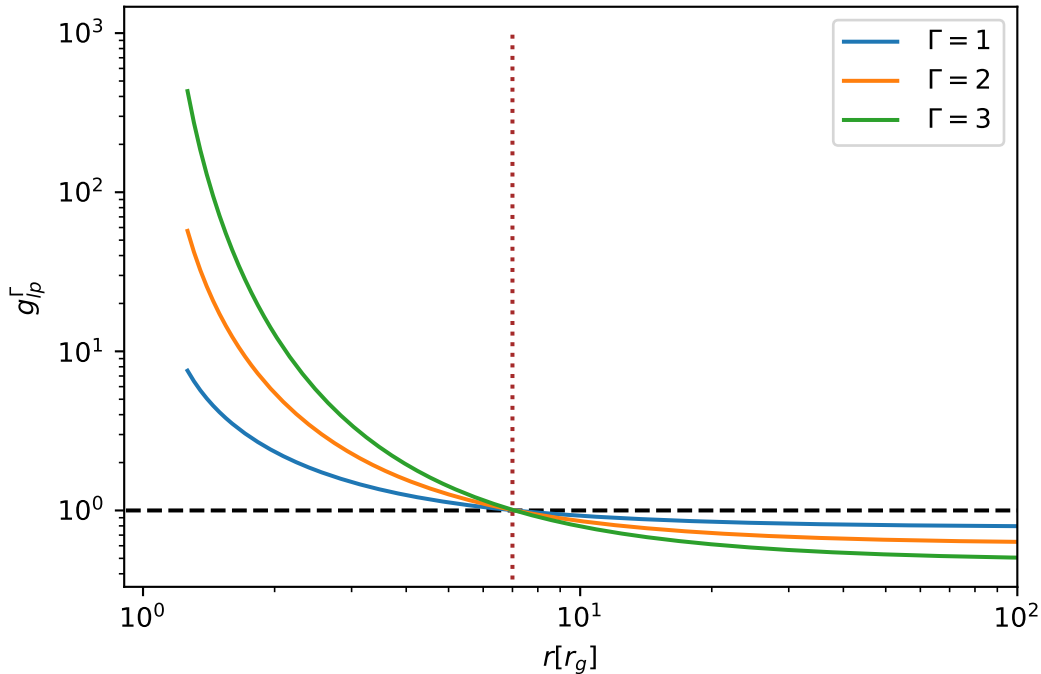

Figure 3.5: The energy shift undergone by photons along the their geodesics from the point of emission to the disk as a function of the incident radius r. For this figure, $a = 0.998$ and $h = 5$. The dashed line represents a ratio of 1, and the dotted line represents the radius at which the ratio of 1 is reached.

Taking the initial four-momentum at the primary source

$$u_h^\mu = (u_h^t, 0, 0, 0) \tag{3.24}$$

and the four momentum on the disc

$$u_d^\mu = u_d^t(1, 0, 0, \Omega) \tag{3.25}$$

as well as the taking the momentum of the photons we can derive the energy relation. The energy shift (Dauser 2010) is

$$g_{\rm lp} = \frac{E_i}{E_e} = \frac{p_\mu u_d^\mu}{p_\nu u_h^\nu} = \frac{(r\sqrt{r} + a)\sqrt{h^2 - 2h + a^2}}{\sqrt{r}\sqrt{r^2 - 3r + 2a\sqrt{r}}\sqrt{h^2 + a^2}}. \tag{3.26}$$

That the geometric effects are most concentrated in the inner radii, can also be seen in Figure 3.5, and this effect increases as the photon index increases. Not only are the largest shifts most concentrated in the inner radii, which one can readily understand as the gravitational well is most powerful near the black hole, but at a radius of approximately $r_g \approx 7$, assuming a source at $h = 5$, we can see that there is an equilibrium where the energy remains constant. To understand this better, if one were to imagine the gravitational field generated by a black hole with no angular momentum. The potential energy of a particle at $5r_g$ above the black hole, and at the same distance along the accretion disk are the same. The angular momentum breaks this symmetry, but the effects of this broken symmetry are only appreciable at the innermost radii. Now that all of the relativistic effects, as well as the energy shift have been determined we can calculate the emissivity profile, shown in Fig. 3.6.
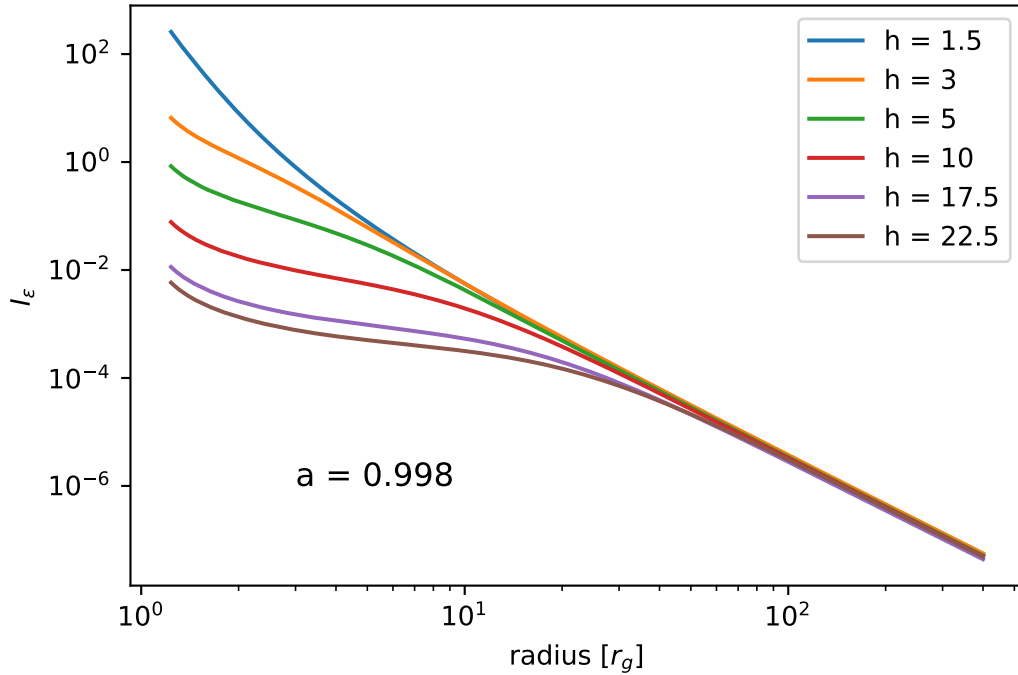

Figure 3.6: Theoretical emissivity profiles of the accretion due to a stationary point source located at on the rotational axis of a black hole (i.e. lamp post model) given in arbitrary units. The height of the point source is varied from 1.5 to 22.5.

4 Radially Extended Lamp Post

After having covered the `relxill` (García et al. 2014) code, and discussed in particular the lamp post model, we now have a basis of comparison for the ring source. In this chapter I will analyze the emissivity from the ring shaped source in a manner akin to the lamp post model in Chapter 3, then compare its qualities to that of the lamp post model and utilize it to calculate blurred emission lines, as well as combining these emission lines with the `xillver` (García et al. 2013) code. These emission lines, as well as the resulting spectra, will also be compared to those of the lamp post model.

4.1 Data Tabulation and Preparation

In order to make use of the simulations of the ring source done by Licklederer (2019) available for use with the `relxill` kernel, the simulation data was stored in a FITS file which was provided by Licklederer. One change of note from (Licklederer 2019), is a change in the velocity profile. In the simulation the velocity profile has been changed and is no longer the formula given in (Licklederer 2019), as this was in error. The velocity of the source is now calculated using

$$v^\nu = (v^r, v^\theta, v^\phi) = v^\nu \text{ where} \tag{4.1}$$

$$v^\phi = e^{\psi - \nu} \left(\frac{1}{d^{3/2} + a} - \omega \right), \tag{4.2}$$

where d is the radius of the ring source. This new velocity profile was then used by Stefan in the calculation of the FITS table.

Each combination of the black hole spin a, source height h, and ring radius d is a result of 500,000 simulated photons using the modified YNOGK code (Licklederer 2019). The radial grid consists of 199 logarithmically spaced bins from the r_{ms} to $1000 r_g$. For each given value of, h, d, and a, the radial dependence of the photon flux, I_ϵ, and the energy shift, g, are stored. In addition, two further columns contain the q_{disc}, the fraction of total photons which are reflected and q_{esc}, the fraction which escape with no reflection, respectively. They are tabulated for each combination of the corresponding d and h values. A total of 25 linearly spaced a values ranging from -0.998 to 0.998 are stored. Additionally, combinations of 25 d and 25 h values that are logarithmically spaced are tabulated. By default, the h or d ranges from 0 to 35, however if the combination of h and d lead to a source location within the r_{ms} of the black hole for the corresponding a value, then the minimum value would be such that the combination of the two was equal or greater than the r_{ms}. The table is loaded into the `relxill` kernel via the relevant functions in `rellp_extended.c`.

The reflection fraction, R, is then determined by $R = q_{\text{disc}}/q_{\text{esc}}$. The energy shift to the power of the chosen photon index, g^{Γ}, is calculated. The photon flux is read from the table as is the radial grid, and the proper area correction (Eq. 3.17) and Lorentz contraction (Eq. 3.18) are applied. After these geometric considerations are applied, the flux is then promptly multiplied by the energy shift, g, as in Eq. 3.23, with the corresponding photon index, Γ, giving the corresponding emissivity. Once the emissivity is determined, it is then promptly re-binned on a radial grid of 1000 bins. All values in the calculation are interpolated linearly. Once these calculations are completed, the emissivity for the ring source can be integrated into the `relxill` kernel in the same manner as the lamp post.

4.2 Energy Shift

Like with the lamp post model, determining the energy shift is a necessary step in the calculation of the emissivity. It is possible to calculate the energy shift more generally for other sources. The derivations in this section follow closely the work of Licklederer (2019). As the energy shift is the ratio of energies for emitted and observed photons we can take the source location to be our emitter and the disk as our observer. This results in

$$E_{\text{em}} = -p'_{(t)} \qquad\qquad E_{\text{obs}} = -p_{\alpha} u_{\text{obs}}^{\alpha} \qquad\qquad (4.3)$$

where u_{obs} is the velocity of the observer. For ease of calculation we define

$$f_t := \frac{\bar{p}_{(t)}}{p'_{(t)}} = \alpha_t^{(t)} + \alpha_t^{(i)} \frac{p'_{(i)}}{p'_{(t)}} \qquad\qquad (4.4)$$

where $p'_{(t)}$ is the t-component of the four-momentum in the frame of the emitter and $\bar{p}_{(t)}$ is the t-component of the four momentum with respect to the local non-rotating reference frame (LNRF). f_t essentially denotes a Lorentz transformation (Eq. 2.77) of the ratio of t-components of the emitter and LNRF momenta. We can then, using this equation along with the t-component of the LNRF momentum (Eq. 2.71), determine energy of the emitter as

$$E_{\text{em}} = -p'_{(t)} = \bar{p}_{(t)} \frac{p'_{(t)}}{\bar{p}_{(t)}} = E e^{-\nu}(1 - \lambda\omega)\frac{1}{f_t}. \qquad\qquad (4.5)$$

To determine the E_{obs} it is possible to use the form of the disk velocity, Eq. 2.83. However, it may be pertinent to consider cases where the disk velocity is modified because of other physical circumstances. In this way u_{obs}^{α} is kept unrestricted, which allows for the possibility of modifying the disk rotation later without much added effort. Letting $u_{\text{obs}}^{\alpha} = \frac{dx^{\alpha}}{d\tau}(u^t, u^r, u^{\theta}, u^{\phi})$, with τ as the observer's proper time, and using Eqs. 2.71-2.74

the observed energy is expressed as

$$sE_{\text{obs}} = E\left(u^t + \text{sign}(r)\frac{\sqrt{V_r}}{\Delta}u^r + \text{sign}(\theta)\sqrt{V_\theta}u^\theta + \lambda u^\phi\right) \tag{4.6}$$

$$= Eu^t\left(1 + \text{sign}(r)\frac{\sqrt{V_r}}{\Delta}\frac{dr}{dt} + \text{sign}(\theta)\sqrt{V_\theta}\frac{d\theta}{dt} + \lambda\frac{d\phi}{dt}\right). \tag{4.7}$$

We can then express the energy shift as

$$g = \frac{E_{\text{obs}}}{E_{\text{em}}} = \frac{\left[u^t\left(1 + \text{sign}(r)\frac{\sqrt{V_r}}{\Delta}\frac{dr}{dt} + \text{sign}(\theta)\sqrt{V_\theta}\frac{d\theta}{dt} + \lambda\frac{d\phi}{dt}\right)\right]_{\text{obs}}}{\left[e^{-\nu}(1 - \lambda\omega)/f_t\right]_{\text{em}}} \tag{4.8}$$

where the brackets indicate that the expression should be evaluated at the position of the observer/emitter respectively. Assuming that disk only moves in the equatorial plane, i.e. $\frac{dr}{dt} = \frac{d\theta}{dt} = 0$. We can then determine the general energy shift for the disk,

$$g = \frac{\left[u^t_{\text{disk}}(1 - \lambda\Omega)\right]_{\text{obs}}}{\left[e^{-\nu}(1 - \lambda\omega)/f_t\right]_{\text{em}}}, \tag{4.9}$$

where ω and Ω are the rotational velocities of the ring source and accretion disk, respectively.

For a given parameter combination of a, d, and h, the energy shift for each individual simulated photon is calculated using Eq. 4.9. Due to the axis-symmetry of the lamp post source, it is possible to analyitcally determine the energy shift value corresponding to a given radial bin. However, for the ring source, there can be photons in the same radial bin which vary in their energy shifts, due to their differing initial positions and direction along the ring source. As a result, it becomes necessary to use the average energy shift in the ring source case.

In order to make the photon index, Γ, a parameter available for fitting in the `rellineExt` and `relxillExt` models, it is necessary to implement a particular method of determining the average energy shift for a given parameter combination. In principle, for a given radial bin, one would simply take the average energy shift of the individual photons in the radial bin, r_i, each to the power of the appropriate photon index, expressed aptly as

$$g^\Gamma_{\text{avg}}(r_i) = \frac{1}{N}\sum_{k=0}^{N} g^\Gamma_k(r_i). \tag{4.10}$$

As stated in the previous section, however, each parameter combination consists of a simulation of many photons, which must be run for each combination of parameters h, d, and a, and consequently store the energy shift information for each photon. For this reason, it is impractical to generate such tables, as they would be much too large. In the table generated for use in `relxillExt`, with nearly 200 radial bins, this means that the energy shifts of roughly 2,500 photons must be stored for every radial bin.

Instead, for a given radial bin, the photons are sorted in ascending order of energy shift, and divided into N equally sized groups g_n. For each group the average photon

energy shift, $\langle g_n \rangle$, is tabulated. The average energy shift for a given photon index, Γ, and radial bin, r_i is then determined by

$$g_{\mathrm{avg}}^{\Gamma}(r_i) = \frac{1}{N} \sum_{n=0}^{N} \langle g_n \rangle^{\Gamma}(r_i), \tag{4.11}$$

where here N is the number of groups, $\langle g_n \rangle$ is a group of averaged photon energy shifts, and Γ is the photon index. The table utilized by `rellineExt` and `relxillExt` contains 20 groups per radial bin. It is, however important to note that this calculation does not give the "true" average energy shift but rather an approximation of the average of the "raised" energy shift. This is the quantity by which the photon flux is multiplied by in Eq. 3.23, and the one which is relevant for determining the emissivity.

4.3 Emissivity

Having found a practical way of determining the energy shift of the ring source, we can now determine its emissivity, which is necessary to calculate the line profiles and subsequently the reflected spectra. Since the Kerr-spacetime is axis-symmetric this suggests that a source extended outward from the rotational axis of the black hole should also exhibit axis-symmetry. For this reason the emissivities presented here were calculated assuming a source with a ring shaped geometry. Due to the source's axis-symmetry, each point source along the ring will produce the same flux and intensity on the disk, only being shifted along the ϕ coordinate. In this case, it is possible to simply simulate a single point source and to project the resulting spectrum onto the radial coordinate. A similar treatment was done in (Wilkins & Fabian 2012).

As was the case for the lamp-post model, the parameters h and a denote the height of the source above the black hole and the black hole's spin respectively. However, in addition to these parameters, I introduce d which represents the distance of the source from the rotational axis. The parameters d and h can be related to the Boyer-Lindquist coordinates r and θ by

$$d = \sqrt{r^2 + a^2} \sin \theta \tag{4.12}$$

$$h = r \cos \theta. \tag{4.13}$$

For smaller values of d only minimal differences between the lamp post are to be seen, however for values where $d \geq h$ a substantial increase in the flux at $r \approx d$ can be observed, while the rest of the emissivity follows a similar pattern, as in the case of the lamp post model, as seen in Fig. 4.1. The sharp peak at $r \approx d$ is readily explained by an increase in the photon flux due to its vicinity of the radiating source. The peaks also increase in magnitude for increasing distance from the black hole, which can be explained by the decreased strength of the gravitational field at distances farther from the black hole.

Because of these assumptions however, one would expect that if the radius of the ring is decreased, we should slowly recover the same results as that of the lamp post model. Comparing the ring source for $d = 0$ should yield equivalent results to the lamp post
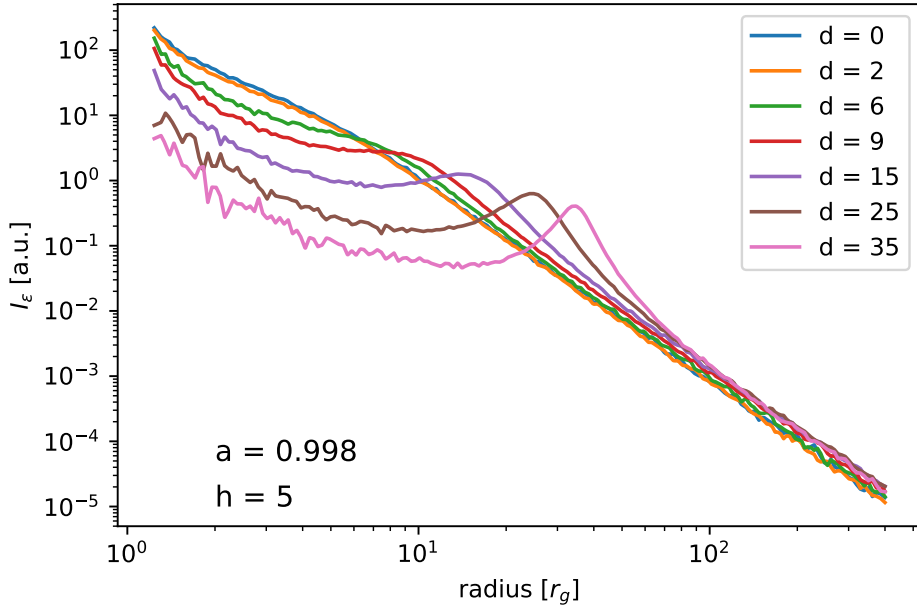
Figure 4.1: Emissivity profiles for varying ring distances from the axis of symmetry. With a height of $h = 5.0$ and spin of $a = 0.998$. A significant feature is the increase around $r \approx d$, gradually increasing in significance at larger radii. The emissivities are given in arbitrary units.
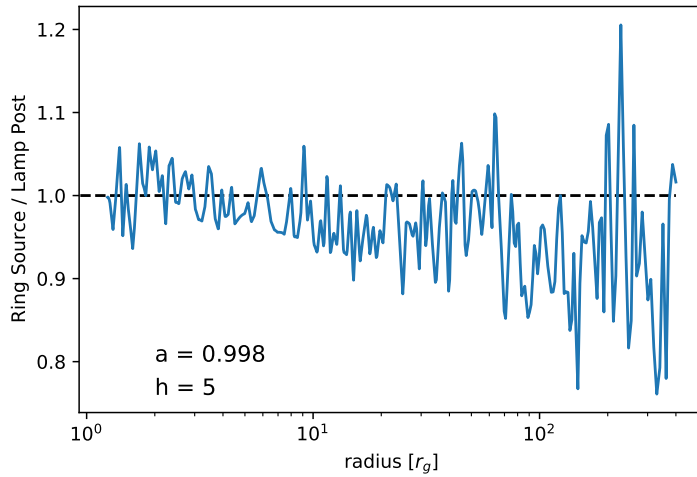

Figure 4.2: The emissivity of made use of in the lamppost models in relxill compared to that used in the extended source with $d = 0$. A ratio of the ring source compared to the lamp post model. For both models the parameters $a = 9.88$ and $h = 5$ were used.

model. Fig. 4.2 illustrates that the two models indeed agree relatively well. In the inner regions they are within a roughly 5% difference of the lamp post model. For higher radii the difference is larger however the most relevant contributions to the spectra from the emissivity are those in the inner regions and here the accuracy can be considered sufficient, and in principle the accuracy can be increased by increasing the number of photons in the simulation used to tabulate the data.

4.4 Line Profiles

After the determination of the ring source emissivity I then integrated it for use in the `relxill` kernel, thereby creating the new `rellineExt` and `relxillExt` models. Here I will determine the line profiles and compare them to those of the lamp post model. Before I examine the effect of the new ring radius parameter, d, I will compare the ring source model, with $d = 0$, to the lamp post model. Because a ring with no radius coincides with a point, the two models should coincide. As with the lamp post model, the ring source is very sensitive to changes in the height of the source (Figs. 4.3a and b), as well as to changes to the photon index, Γ. The same behavior can be seen for
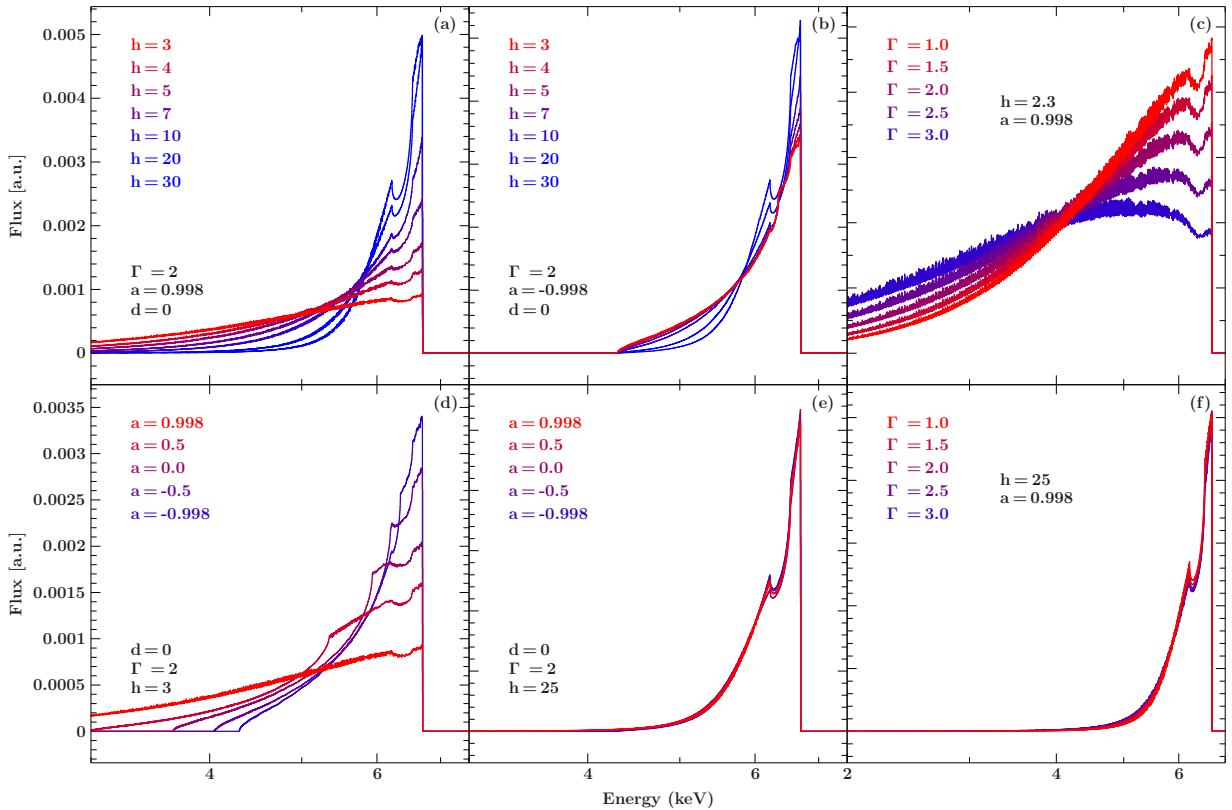

Figure 4.3: Line profiles of the `rellineExt`, each varying particular parameters, from Γ, to a. Unless otherwise stated, the default `relxill_lp` parameter values are used.

the negatively spinning black hole, albeit to a lesser degree (Fig. 4.3b). Sources near a highly rotating black hole also vary immensely with a change in the photon index of the input spectrum (Fig. 4.3c). For varying photon indices, the lines profiles are quite noisy. This may be an issue from the particular method for determining the energy shift, and may possibly be alleviated by increasing the number of groups in Eq. 4.11. For sources near the black hole, the model is also sensitive to the spin, with a substantial narrowing of the line shape occurring for non-rotating and negatively rotating black holes (Fig. 4.3d). However, for sources located farther from the black hole along the axial direction, the sensitivity of the line shape to nearly all parameter values vanishes. At $h = 25$ the different parameter combinations produce nearly indistinguishable line shapes (Fig. 4.3e and f), but even with heights as small as 10 r_g the sensitivity to parameters such as the spin and photon index are drastically reduced.

Fig. 4.4 shows that discrepancies of two parameter combinations, when compared to the `relline_lp` model. The value of $h = 2.3$ corresponds to a value directly tabulated the FITS file, meaning no values were interpolated. The value of $h = 2$ is located roughly halfway between two containted values in FITS file, allowing us to assess the accuracy of interpolated values. It can be seen that for directly tabulated values, the `rellineExt`
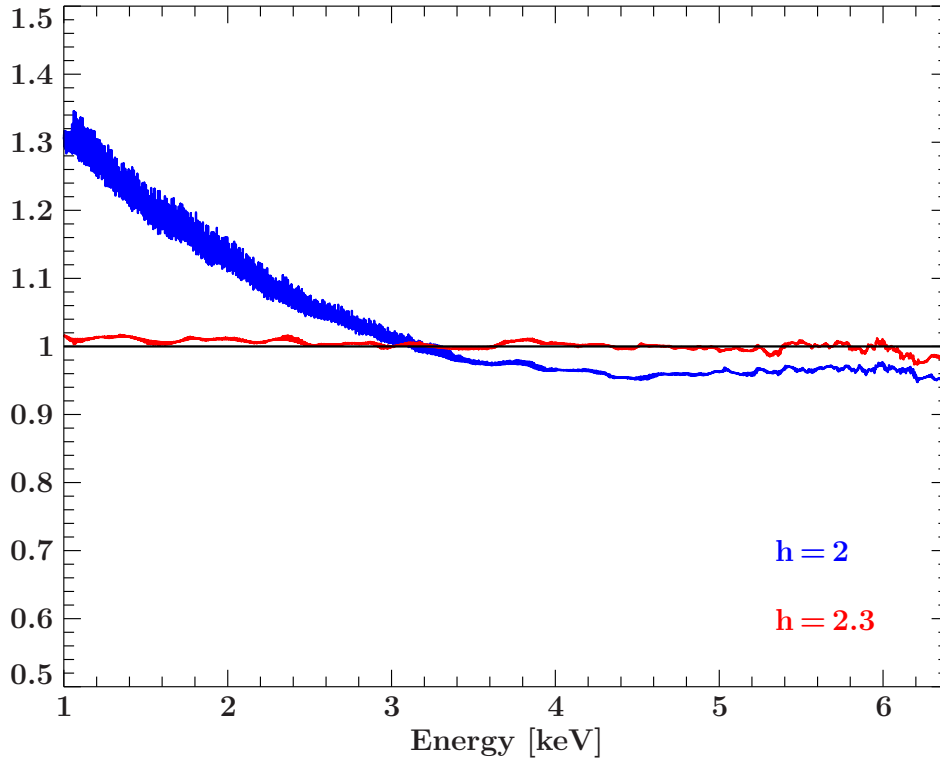

Figure 4.4: The blurred emission line varying the values of *d*. The default parameter values in `relline_lp` are used with $a = 0.998$ and $h = 2$. The ring source model is compared to that of the lamp post, `relline_lp`, in black.

model agrees incredibly well, with deviations less than 2% for nearly the entirety of the iron line. However, when interpolating to values furthest away from nearest tabulated

values, a significant degree of error, upwards of 30% is observed, primarily for the lower energies. While this error is indeed great, it represents the likely maximum possible error, as the error will likely decrease the closer a tabulated value. This may pose significant problems for the results in this thesis, but also points to logically straight-forward, if not necessarily practical solution for this inaccuracy.

Having observed that the ring source reproduces behaviors of the lamp post model for $d = 0$, I now analyze the effect of the newly introduced ring radius, d. As illustrated in Fig. 4.5, an increased radius of the ring serves to narrow the emission line. The broadened shape of the line is more present at higher ring radii, and gradually narrows with increasing distance from the rotational axis. The characteristic double peak shape of the `relline_lp` (Dauser 2010), seen in Fig. 4.5 in black, is still present. However, at larger ring radii this fades. The effect of increasing d narrows the line in a similar fashion to increasing the height, h of the source along the rotational axis (Fig. 4.3a). Drastically increasing the radius of the ring source, such as $d = 25$, while keeping the
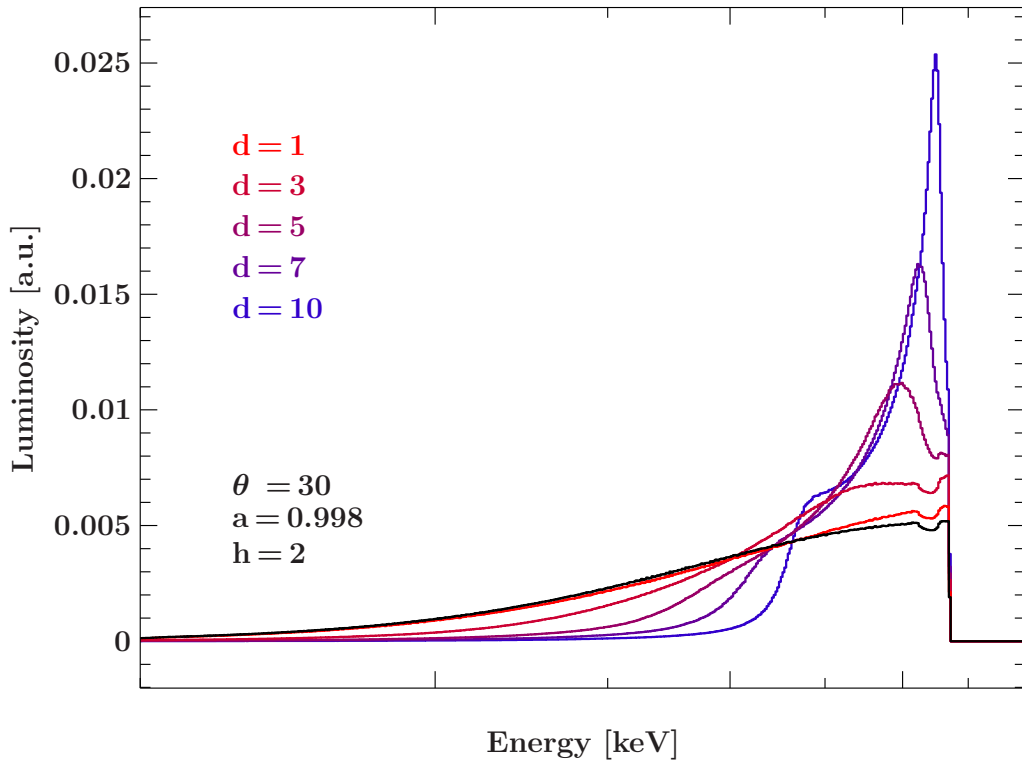

Figure 4.5: The blurred emission line varying the values of d. The default parameter values in `relline_lp` are used with $a = 0.998$ and $h = 2$. The ring source model is compared to that of the lamp post, `relline_lp`, in black.

height relatively low makes apparent a sharply asymmetric double peak shape (Figs. 4.3h, and i). This effect can also be seen for negatively spinning black holes, however, much like height variation, it significantly diminished (Figs. 4.6b,e and h). In a similar fashion, the greatest sensitivity of the model to parameters can be seen when the source is closest to the black hole. At small ring radii, the deviation of the shape from that of

a point source is quite low (Figs. 4.6a-c) while variation can still be seen with varying source height (Fig. 4.6d). Similarly to Fig. 4.3c, for varying photon index, the line profiles are quite noisy, suggesting this issue is persistent with lower values from d as it appears more sharply for higher d values (Figs 4.6c,f, and i). At intermediate disk radii i.e. $d = 10$, the line shapes from various spin and photon indices begin to rapidly coincide (Figs. 4.6e and f), and at $h = 25$ r_g the difference is practically indistinguishable for all parameter combinations. However, even at very large disk radii, the line shape exhibits notable sensitivity to changes in the height of the source.
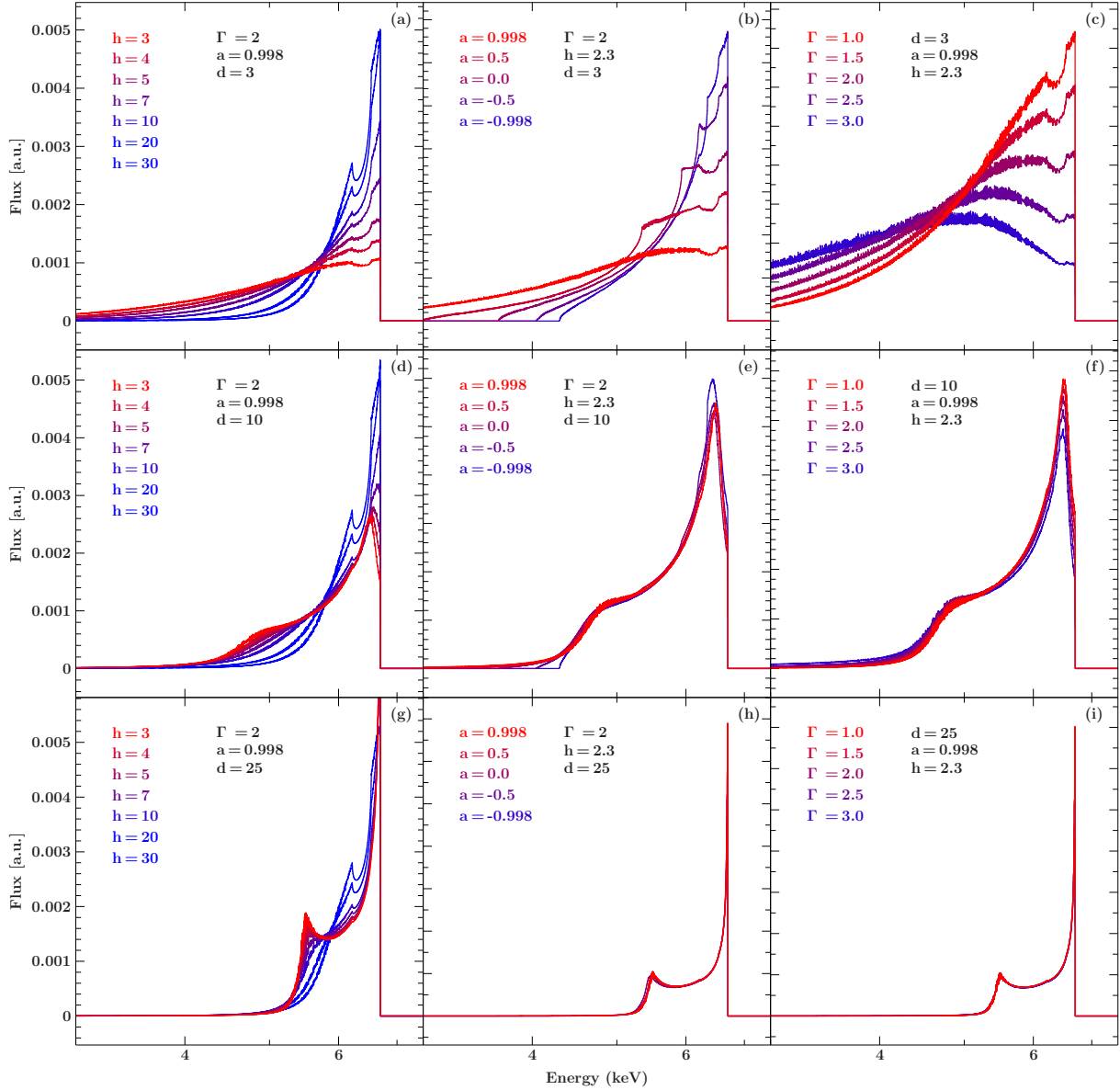

Figure 4.6: Line profiles of the `rellineExt`. Unless otherwise stated, default parameter `relline_lp` values are used.

As the source is no longer assumed to be along the rotational axis of the black hole,

one might expect to see differing behavior along the azimuthal direction. From Fig. 4.7 it can be seen that, for less compact sources, the greatest increase in luminosity occurs not for the highest inclination, but rather the most luminous peak is observed at lower inclinations, in this case $d = 8$ causes a greater luminosity at $\theta \approx 50$. In addition to the shifted luminosity, a great distortion in the shape of the emission can be observed and this distortion appears asymmetric with respect to peak observed at $\theta \approx 50$.

The increased ring radii narrow the line shape, much like the introduction of a source elongated along the rotational axis (Dauser et al. 2013). In a manner similar to an elongated source, the problem of ambiguity in the measurement of the black hole spin arises. If a narrow line is measured, it is not necessarily possible to assume that narrow shape is a result of a low-spin. The shape could be a result of a small and compact source near a slowly spinning black hole, or it could be a quickly rotating black hole with a ring source of large radius. The contrary to this, is that if one is able to independently determine the spin of the black hole, such as with X-ray continuum spectroscopy (Steiner et al. 2011) or time-domain very long baseline (VLBI) observations of in-falling gas clouds (Moriyama et al. 2019), one can more accurately determine the precise geometry of the source.
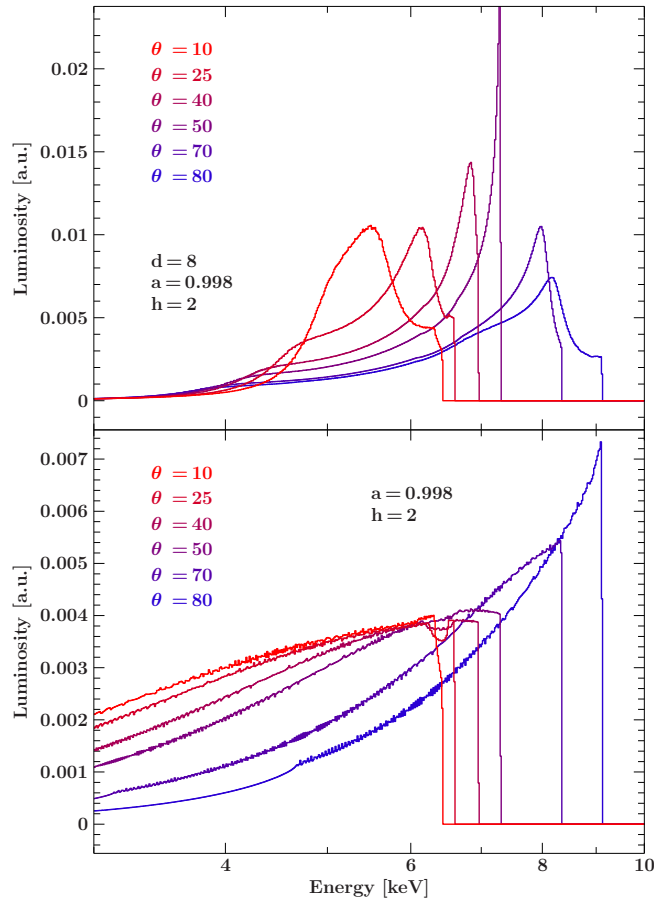

Figure 4.7: The blurred emission lines with the ring source (above) and lamp post (below) emissivities varying the values of θ with $a = 0.998$, $h = 2$ and $d = 8$.

4.5 Reflection Spectra

While the newly created `rellineExt` model lets us model and analyze line profiles and determine the effect of a radially extended ring source on its broadened shape, in order to determine the effect this will have on the larger X-ray spectrum, it is necessary to combine these line profiles with the `xillver` (García et al. 2013). Using the newly created `relxillExt`, which implements the `relxill` kernel using the emissivity from the previously discussed ring source we can compare the results to the corresponding lamp post source. As illustrated in Fig. 4.8, the effect of blurred emission lines become clear. The increased distance from the source, as expected from analyzing the line shape,
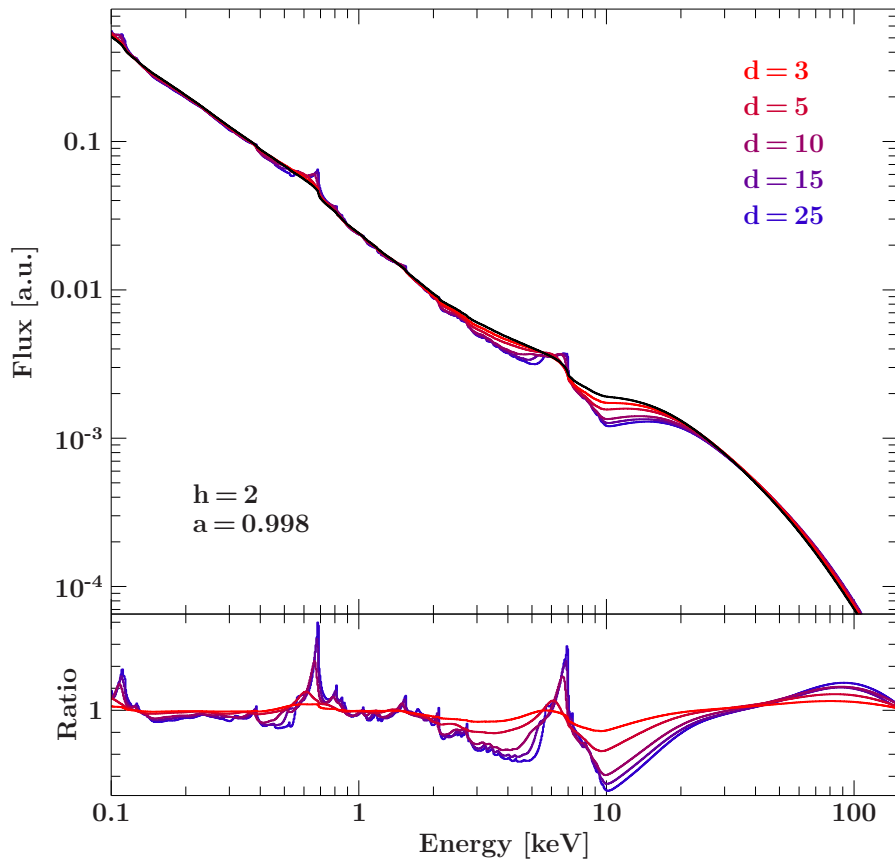

Figure 4.8: Comparison of the reflected spectrum of the ring source model with that of the lamp post (in black) with varying d values for $h = 2$ and $a = 0.998$. All other parameters use their default values unless otherwise stated.

narrows the emission peaks in the overall spectrum. In addition a sharp dip can be observed before the Compton hump. When varying parameters for the `relxillExt`, sensitivity of the spectrum to the height can be seen in the in Figs. 4.9a, 4.9d, and 4.9g. Sensitivity can also be seen in the spin, a, parameter can be seen for Figs. 4.9b, 4.9e, and 4.9h. Additionally sensitivity is observed for the photon index, Γ, Figs. 4.9c, 4.9f, and 4.9i. With respect to all other parameters, the effect of the d is seemingly clear. The
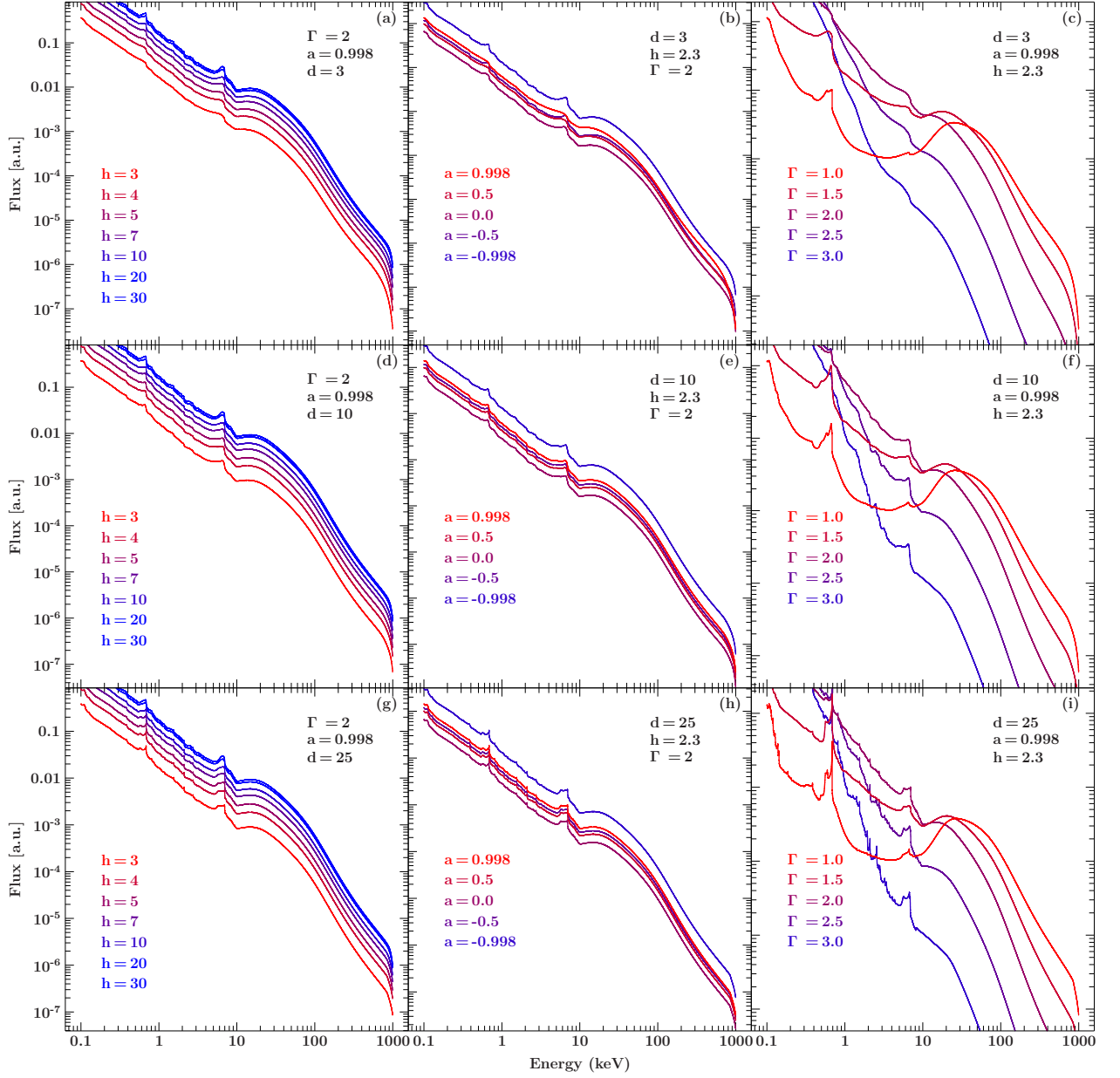
Figure 4.9: Comparison of the reflected spectrum of the ring source model with that of the lamp post (in black) with varying d values for $h = 2$ and $a = 0.998$. All other parameters use their default values unless otherwise stated.

narrowing of the emission lines can be seen in Figs. 4.9, and appears and comparatively little sensitivity to the other parameters can be seen.

5 Analyzing Reflected Spectra

With the `relxillExt` model fully constructed and in working order it can be implemented in the X-ray analysis of a black hole source. Although this model can in principle be applied to any source which is believed to be a black hole, the choice of source is relevant in order to more succinctly explain observations that are less clear from existing models, like the lamp post model. To that end, Markarian 335 (Mrk 335) was chosen for this analysis. I will first discuss this source and the reason for its selection, then summarize the analysis of the source, and finally discuss the results.

5.1 Markarian 335

Mrk 335 is a narrow-line Seyfert 1 galaxy with a redshift of $z = 0.026$ and mass of $2.6 \times 10^7 M_\odot$ (Grier et al. 2012). Observations from 2000 to 2006 indicated the presence of a bright X-ray source in a high flux state. Regular observation of this source with the *Swift* satellite has been occurring since 2007 and found that the flux had subsequently dropped by a factor of 10 since 2006 (Grupe et al. 2007). The X-ray spectra ranging from early high flux observations (Crummy et al. 2006; Grupe et al. 2008) to low- (Grupe et al. 2008) and even much later intermediate-flux (Gallo et al. 2013) states can be explained by X-ray continuum emission from a corona of highly energetic particles which surround the black hole and illuminate the accretion disk (George & Fabian 1991). This causes X-ray reflection via Compton scattering, photoelectric absorption and the emission of fluorescence lines and as well as bremsstrahlung (Ross & Fabian 2005). The resulting reflection spectrum, particularly the 6.4 keV Kα emission line, is blurred by Doppler shifts and relativistic distortion caused by the orbital motion of accretion disk in addition to gravitational redshifts as a result of the strong gravitational field near the black hole (Fabian et al. 1989; Laor 1991) where the corona contracted to $12r_g$ and $5r_g$, respectively (Wilkins & Gallo 2015). An analysis by Wilkins & Gallo (2015) concluded that the in the low flux state, accretion disk was illuminated by a corona extending out to a $26^{+10}_{-7}r_g$ covering the inner regions of the accretion disk. Additionally it was concluded that the corona contracted to $12r_g$ and $5r_g$ for the intermediate- and low-flux states, respectively. The high degree of variability in the flux and the measured shift in the radial extent of the corona makes Mrk 335 a prime candidate for studying how energy is freed from accretion flow in active galactic nuclei (AGN), in addition to the change in radial extent measured by (Wilkins & Gallo 2015).

5.2 Spectral Analysis

Having selected the proper source, we can conduct the spectral analysis in this section. I make use of data from the 75 ks *NuSTAR* observation on 2014 September 20 (*NuSTAR* OBSID 80001020002), using the FPMA and FPMB detectors, which corresponds to the measured value of $d = 5r_g$ as measured by Wilkins et al. (2015). Using `isis` (Houck & Denicola 2000) the spectra were binned with at least 20 counts per spectral bin and a minimum signal-to-noise ratio of 2. This choice of binning allows us to use the χ^2 statistic to assess the goodness of fit of the `relxillExt` model. Due to a not yet resolved issue with the normalization of the `relxillExt`, only the reflected component of the model was used by setting the parameter `fixReflFrac` = 3. This reflected component was then added to a power-law spectrum with a high energy cutoff instead, with the high-energy cutoff and photon index Γ tied to the same values as the `relxillExt` model, or in the language of `isis`,

$$\text{tbnew\_simple} \times (\text{relxillExt} + \text{cutoffpl}).$$

The disadvantage of this method is that it is no longer possible to extract information about the reflection fraction.

Given the availability of a previous analysis using the `relxill_lp` model, this analysis began starting with best fit parameters obtained there. Following (Wilkins et al. 2015), the inclination was frozen at $\theta = 57.1°$ as well as the hydrogen abundance $N_H = 3.6 \times 10^{20} \text{cm}^{-2}$ for modeling galactic absorption. In an attempt to recreate the best fit with the `relxillExt` model for the lamp post case, the ring source radius parameter, d, was initially frozen at $d = 0$. Using the same parameter values as in Wilkins et al. (2015), I obtained a goodness of fit of $\chi^2/\nu = 1.08$, compared to the 1.02 given by Wilkins et al. (2015). The upper bound for the source height, $h = 2.1$, given in Wilkins et al. (2015) was then set as the upper soft limit of the h in `relxillExt` and allowed to fit freely, while keeping other parameters frozen. However, this did not improve the fit. Allowing the parameters to vary freely, I was able to obtain a better fit, with a goodness of fit of $\chi^2/\nu = 1.06$. The best fit parameters are listed in Table. 5.1. The spin parameter was frozen at $a = 0.998$, for both $d = 0$ and when fitted freely. this was done as initial fits showed essentially no change in the spin (i.e. $a > 0.99789$). In addition Wilkins et al. (2015) did not find evidence of truncation of the inner disk, and the measured value $r_{in} = 1.235r_g$ corresponds to the r_{ms} for $a = 0.998$, confirming the validity of freezing the spin parameter. The best fit parameters obtained in this case differ slightly from those in Wilkins et al. (2015). The spectrum is slightly softer, with a reduced photon index, although contained with the error margins of the Wilkins et al. (2015) measurement. The ionization value lies within the lower bound of $\xi < 53$ given by Wilkins et al. (2015). However this parameter is not very well contained due to its large error margins. The iron abundance A_{Fe} significantly increases. While it is contained within the margin of error of the Wilkins et al. (2015) result, it is however, near the upper limit.

Once a best fit was achieved with $d = 0$, the parameter was allowed to fit freely in order to obtain the best fit for the ring source. Compared to the result with d fixed at 0, we can see a further softening of the spectrum with a slightly reduced photon index, Γ.

Table 5.1: Best fitting model parameters to the *NuSTAR* spectrum of Mrk 335 fit in the range of 3-50 keV.

Parameter	`relxillExt` with $d = 0$	`relxillExt`
$h \; [r_g]$	$1.84^{+0.06}_{-0.09}$	< 1.3
$d \; [r_g]$	0^f	$2.17^{+0.23}_{-0.12}$
a	0.998^f	0.998^f
Γ	$2.460^{+0.008}_{-0.012}$	$2.414^{+0.018}_{-0.016}$
$\log \xi$	$0.3^{+1.5}_{-0.3}$	$0.3^{+1.4}_{-0.3}$
$A_{\mathrm{Fe}} \; [solar]$	$3.26^{+0.57}_{-0.26}$	$3.33^{+0.08}_{-0.26}$
χ^2/ν:	1.06	1.04

The ionization value also lies within the lower bound of $\xi < 53$ given by Wilkins et al. (2015). However, as with the case with fixed $d = 0$, the measured ionization has a wide margin of error. While the best-fit result for the height in the freely fitting model is $1.3r_g$, this was a result of the hard lower limit that was set to ensure computational viability. It is necessary that, for any combination of a, d, and h, the location of the source from the black hole center is greater than the r_{ms}. For a maximally spinning black hole, with an r_{ms} of $1.24r_g$, the combination of $h = 1.3$, $d = 2.2$ leaves little room for error. It is possible that a general source might be incredibly radially extended but at heights lower than the r_{ms}. Originally the hard limit was set much lower, but after having `relxillExt` crash multiple times during fitting, the hard limit was raised to $1.3r_g$. For this reason, the best-fit height of $1.3r_g$ may not be reflective of the source's true height, but should serve as an upper limit of the source height.

5.3 Discussion

The model fits rather consistently with goodness of fits, χ^2/ν, of 1.06 and 1.04 for the $d = 0$ and freely fitting d, respectively. All freely fitting `relxill` parameters fit within the margin of error obtained by Wilkins et al. (2015). However, they do not a fit as accurately as the Wilkins et al. (2015) results, where a goodness of fit of 1.02 was obtained for using `relxill_lp`. In the analysis from Wilkins et al. (2015), out-flowing absorption components were modeled using the photo-ionization code `xstar`, where a best fit improvement of $\Delta\chi^2 = 16$ (with two additional free parameters) was obtained. Whether this would have closed the gap in the difference between the results from Wilkins et al. (2015) and my results is not known, but their inclusion in my analysis would have most likely improved the goodness of fit. Additionally, *Suzaku* observations of Mrk 335 from 2013 and 2006 indicate that the most likely explanation which explains the long-term and rapid variability of Mrk 335 (Gallo et al. 2015) is a rapidly spinning black hole ($a > 0.91$), which provides further justification for the decision to freeze $a = 0.998$.

In Wilkins et al. (2015), the upper bound for the height, h, of the lamp post source was found to be $2.1r_g$ from the black hole. For `relxillExt`, keeping $d = 0$, the source of the height was $1.84^{+0.06}_{-0.09}$. This is well within the upper bound of the results from Wilkins et al.
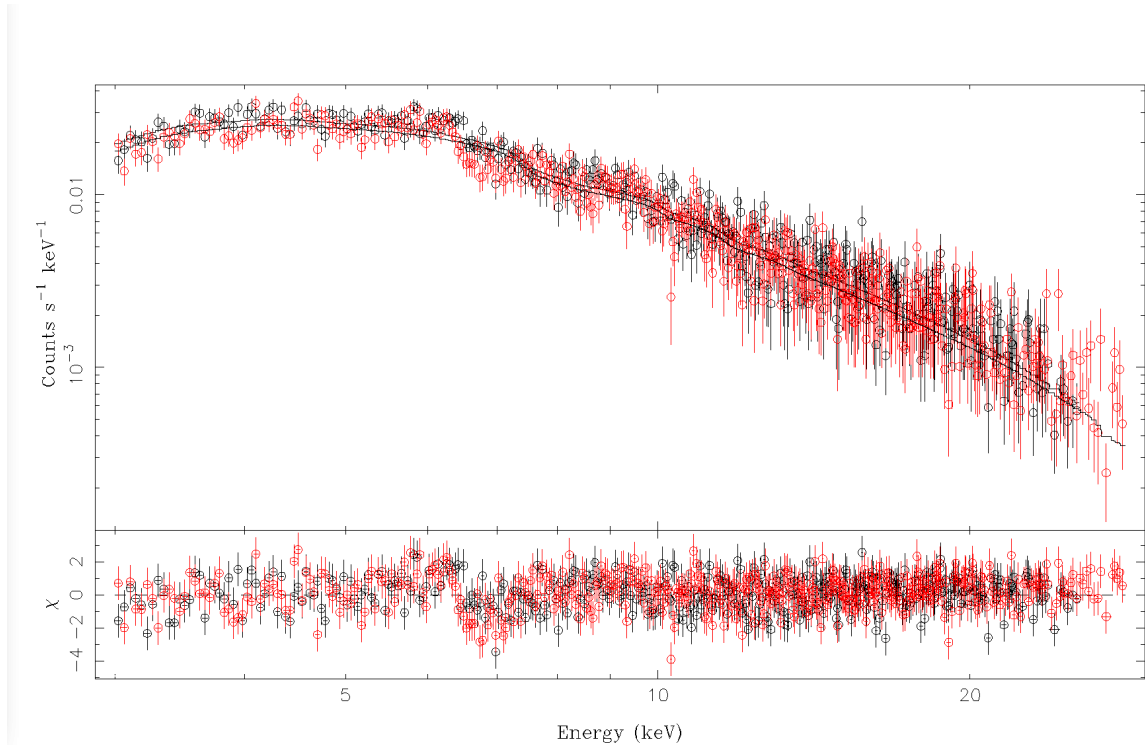
Figure 5.1: X-ray spectra of Mrk 335 measured by *NuSTAR* FPMA and FPMB detectors during the decline of the 2014 flare with the `rexlillExt` reflected spectra best fit, with $d = 0$ fixed.

(2015). When letting d vary freely a upper bound on the height of $h < 1.3r_g$ was obtained. Due to the computational issued mentioned in the previous section, it is possible that the height is lower than the r_{ms}. This would require that the radial extension is sufficiently large such that the position of the ring remains outside r_{ms}. For the case of freely fitting d, a measured value of $2.17^{+0.23}_{-0.12}$ was obtained. In Wilkins et al. (2015), the measured emissivity suggests a compact source with a radial extension no larger than $5.1r_g$ (Wilkins et al. 2015), and the measured value obtained with `relxillExt` lies well within this bound, indicating agreement.

The results are plotted in Figs. 5.1 and 5.2. Since they both describe the data relatively well, they appear very similar. Of note in both figures is the increased discrepancy at approximately 6.4 keV, which indicates the iron line. The low ionization as detected in both cases would decrease the prominence of the iron line, possibly explaining observed behavior of the best fit. This possibly indicates that the fitted value of the ionization is the result of a local minimum. A higher ionization might explain the data more accurately but the fit was not given the possibility of escaping the local "best-fit" value, reflected in the increased residuals near the iron line.
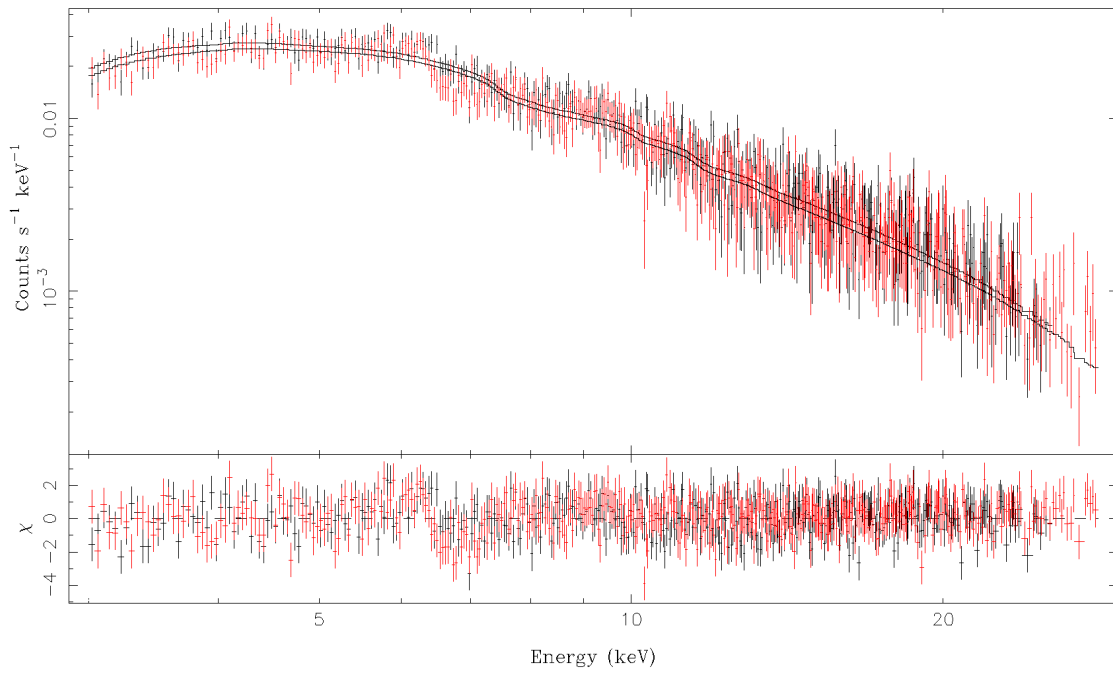
Figure 5.2: X-ray spectra of Mrk 335 measured by *NuSTAR* FPMA and FPMB detectors during the decline of the 2014 flare with the `rexlillExt` reflected spectra best fit, letting *d* fit freely.

6 Conclusion and Outlook

The goal of this thesis was to expand upon the already well-established `relxill` and `relxill_lp` (Dauser 2014) models. By taking photon simulations using the `YNGOK` code (Yang & Wang 2013) for a radially extended ring source the emissivity could be determined (Licklederer 2019). This emissivity was then integrated into the `relxill` kernel allowing for the creation of `rellineExt`, for the modeling of broadened emission lines, and `relxillExt`, for the determination of the angular-resolved spectra. It was shown that, in the appropriate limit, the ring source model reduces to lamp post model and exhibits the same parameter sensitivities for this limited case. Just as extending the reflection model for the lamp post geometry made it possible to probe the geometry of the source rather than fitting an artificial emissivity, the introduction of a ring source model as presented in this thesis opens up the possibility to more accurately determine the precise geometry of the irradiating source.

The effect of the newly introduced source geometry is to narrow the emission line as discussed in Section 4.4. For large values of ring radius ($d \geq 25$) a strongly asymmetric double peak shape is seen. Additionally it provides the ability to narrow the emission line in a manner which does not require increasing the height of the source. Instead of a point source which is assumed to be located far from the black hole, the source might instead be located much closer but radially extended from the rotation axis. The analysis of Mrk 335 with `relxillExt` appears to confirm this hypothesis as well, as a source with lower heights and radial extension explained the data just as well as a more distant lamp post source, in fact, slightly better. The obtained disk radius of $d = 2.17^{+0.23}_{-0.12}$ is well within the upper limit of the corona determined by Wilkins et al. (2015). However, the upper limit from Wilkins et al. (2015) was determined by dividing the iron line into contributions from reflection at successive radii (Wilkins & Fabian 2011), unlike the ring source. A continuous disk emissivity of equivalent flux contains more photons in the inner regions near the black hole, than for a ring source. In order to produce a equivalent portion of highly distorted photons, the ring source must be then located closer to the rotational axis, which would bring down the estimated upper limit given by Wilkins et al. (2015). While the result presented in this thesis is promising, a stronger conclusion necessitates a more rigorous analysis.

In addition, it must be taken into account that these results are rather preliminary. There is still a fair degree of discrepancy between the ring source and lamp post emissivity, and the resulting line profiles in the limits where they should theoretically coincide. However, the ability to reproduce the many behaviors of the lamp post in the proper limit, even with limited accuracy, attests to the validity of the approach taken in this thesis.

6.1 Extension to a Disk Source

Though the new `relxillExt` model is not as simple as the lamp post geometry, it is not an extended generalization. The emissivity profiles resulting from more general sources, with thickness both along the rotational axis and perpendicular to it, have been analyzed (Wilkins & Fabian 2012) (see Fig. 6.1). Although emissivity profiles can be and have been extracted from sources such as the Line Seyfert galaxies 1H 0707-495 (Wilkins & Fabian 2012) and Mrk335 (Wilkins et al. 2015) that resemble the extended geometries analyzed by Wilkins & Fabian (2012), no models yet exist, to date, which can calculate the reflected spectra produced by these geometries.

Given the already functional ring source emissivity provided by `relxillExt`, a extended ring source could be effectively simulated by adding together the emissivities emitted by concentric rings, ranging from d_{in} to d_{out} at sufficient density. To add thickness perpendicular to the equatorial plane, the emissivities of successive heights, h_{base} to h_{top}, could be added. As mentioned in the concluding remarks of this thesis, the method of emissivity calculation divides relativistically broadened iron Kα emission line into contributions from reflection at successive disk radii (Wilkins & Fabian 2011), making the obtained ring radius estimate not directly comparable to the results obtained by Wilkins et al. (2015). Implementing the general disk extension would allow us to compare more effectively to the emissivity measurements.
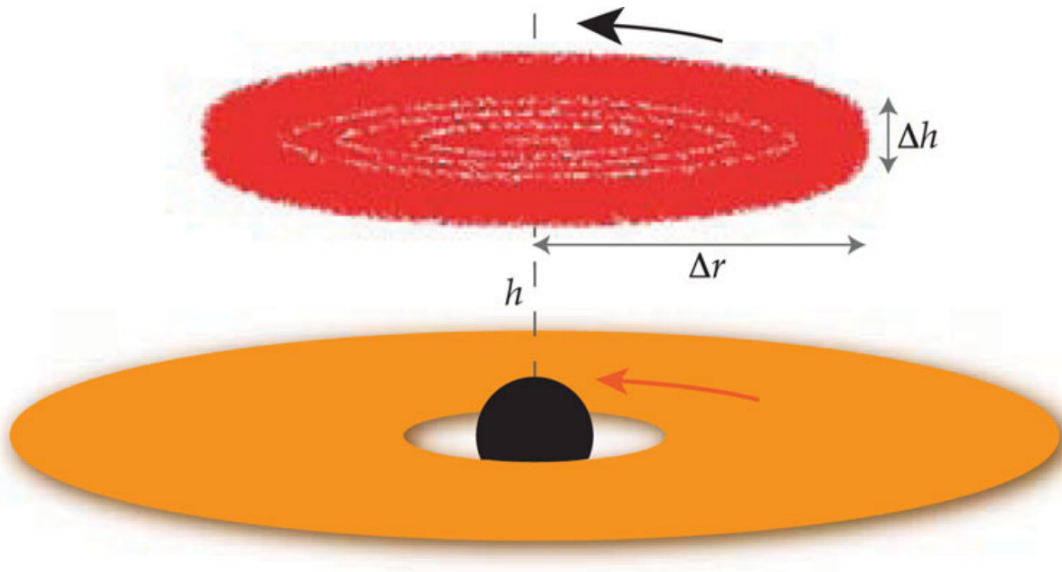

Figure 6.1: Extended X-ray source defined by lower and upper heights from the disc plane and inner and outer radii. Figure taken from Wilkins & Fabian (2012).

6.2 General Accretion Disks

The simulations conducted by Licklederer (2019) that were instrumental to the construction of the `relxillExt` model, were calculated with the assumption that the accretion disk follows the Shakura-Sunyaev Disk (Shakura 1973) model, which assumes that the accretion disk solely inhabits the equatorial plane. However this is not a valid assumption for all cases. Various accretion disk models exist that do not assume a "thin" disk including the "ringed accretion disk" (Pugliese & Stuchlík 2015), "Polish donut", and advection-dominated accretion flows (ADAFs) (Abramowicz & Fragile 2013). Combining the relativistic reflection of `relxill` with the a more refined model of the accretion disk could allow us to better understand the physical processes that radiate energy away from the black hole. This has been done recently for the "Polish donut" model (Riaz et al. 2020), but, as of the date of publication of this thesis, not for the other models.

Acknowledgments

I would like to deeply thank my advisor Jörn Wilms for giving me the opportunity to write my thesis at the Dr. Karl Remeis observatory and for the interesting topic on which this thesis was written. I also appreciate the attempt to make my Master's experience as normal as possible even in the midst of a worldwide pandemic.

I owe a great thanks to my second advisor Thomas Dauser. The entire basis of my work owes its existence to the work done perviously by him. I also would like to thank him for the guidance and advice he gave, especially in the process of writing and structuring my thesis and how to navigate through the `relxill` code. I have definitely learned a lot during this time of conducting this research and the writing of this thesis and will always be grateful for that.

I would like to thank Stefan Lickelderer due to his work which was integral to this thesis. Many of the calculations and data necessary for the creating of my model would not have been possible without him. Even at very inconvenient times, he always went above and beyond what most people would be willing to do. I also enjoyed the conversations we had, of which there most likely would have been more of, had it not been for COVID-19.

I also owe a great deal of appreciation to Amy Joyce who helped me immensely with the X-ray data analysis. She was always very helpful and kind and in addition to providing much needed knowledge and expertise in X-ray analysis, brought along entertaining conversation and humor.

A great deal of thanks I owe to Ole König as well, whose help when trying to debug my code was greatly helpful as well as his comments on my thesis writing, in addition to helping me with the translation of the german language abstract

I would also like to thank my all of my friends, both new and old, who lifted my spirits and gave me the motivation to continue, or simply gave me a temporary respite from the monotony of thesis writing. A particular thanks to Kelly, who has been there for me always, through thick and thin, and Jackson, who always kept me entertained after long days of writing and reading, and was excited to read my thesis at various stages even when most of it seemed like gibberish.

I owe an immense deal of gratitude to my girlfriend, Federica, whose unending support might have quite literally kept me sane. There is unlikely any other person with the unrivaled ability to keep me grounded and my head screwed on properly, even in moments where it would have been easier to let my stress get the better of me.

Lastly I would like to thank my parents, who have always supported me in all of my endeavors and will continue to always do so, and also my sister, who despite being an ocean away, is always there for me. None of what I have accomplished would have been possible with you.

Bibliography

Abramowicz, M. A. & Fragile, P. C. 2013, Living Reviews in Relativity, 16, 1, aDS Bibcode: 2013LRR....16....1A

Arnaud, K. A. 1996, 101, 17, conference Name: Astronomical Data Analysis Software and Systems V ADS Bibcode: 1996ASPC..101...17A

Balbus, S. A. & Hawley, J. F. 1991, The Astrophysical Journal, 376, 214, aDS Bibcode: 1991ApJ...376..214B

Bardeen, J. M., Press, W. H., & Teukolsky, S. A. 1972, The Astrophysical Journal, 178, 347, aDS Bibcode: 1972ApJ...178..347B

Boyer, R. H. & Lindquist, R. W. 1967, Journal of Mathematical Physics, 8, 265, aDS Bibcode: 1967JMP.....8..265B

Brenneman, L. W. & Reynolds, C. S. 2006, The Astrophysical Journal, 652, 1028, aDS Bibcode: 2006ApJ...652.1028B

Brenneman, L. W., Reynolds, C. S., Nowak, M. A., et al. 2011, The Astrophysical Journal, 736, 103, publisher: American Astronomical Society

Byram, E. T., Chubb, T. A., & Friedman, H. 1966, The Astronomical Journal, 71, 379, aDS Bibcode: 1966AJ.....71..379B

Caballero-Garcia, M., Dovčiakdovˇdovčiak, M., Papadakis, I., et al. 2016, PoS (Proceedings of Science)

Carlson, B. C. 1989, Mathematics of Computation, 53, 327

Carlson, B. C. 1991, Mathematics of Computation, 56, 267

Carlson, B. C. 1992, Mathematics of Computation, 59, 165

Carlson, B. C. 1995, Numerical Algorithms, 10, 13

Carroll, S. M. 2004, Spacetime and geometry. An introduction to general relativity, publication Title: Spacetime and geometry / Sean Carroll. San Francisco ADS Bibcode: 2004sgig.book.....C

Carter, B. 1968, Physical Review, 174, 1559, publisher: American Physical Society

Carter, B. 1971, Physical Review Letters, 26, 331, aDS Bibcode: 1971PhRvL..26..331C

Bibliography

Chandrasekhar, S. 1983, The Mathematical Theory of Black Holes (Clarendon Press and Oxford Univ. Press, Oxford)

Clark, G. W., Lewin, W. H. G., & Smith, W. B. 1968, The Astrophysical Journal, 151, 21, aDS Bibcode: 1968ApJ...151...21C

Crummy, J., Fabian, A. C., Gallo, L., & Ross, R. R. 2006, Monthly Notices of the Royal Astronomical Society, 365, 1067

Cunningham, C. T. 1975, The Astrophysical Journal, 202, 788, aDS Bibcode: 1975ApJ...202..788C

Dauser, T. 2010, Diploma Thesis

Dauser, T. 2014, PhD Thesis

Dauser, T., Duro, R., Wilms, J., et al. 2010, 38, 8, conference Name: 38th COSPAR Scientific Assembly

Dauser, T., Garcia, J., Wilms, J., et al. 2013, Monthly Notices of the Royal Astronomical Society, 430, 1694

Dauser, T., García, J., Parker, M. L., Fabian, A. C., & Wilms, J. 2014, Monthly Notices of the Royal Astronomical Society: Letters, 444, L100

Dauser, T., García, J., Walton, D. J., et al. 2016, Astronomy and Astrophysics, 590, A76

Dexter, J. & Agol, E. 2009, The Astrophysical Journal, 696, 1616, aDS Bibcode: 2009ApJ...696.1616D

Einstein, A. 1916, Annalen der Physik, 354, 769, aDS Bibcode: 1916AnP...354..769E

Everitt, C. W. F., DeBra, D. B., Parkinson, B. W., et al. 2011, Physical Review Letters, 106, 221101, arXiv: 1105.3456

Fabian, A. C., Rees, M. J., Stella, L., & White, N. E. 1989, Monthly Notices of the Royal Astronomical Society, 238, 729, aDS Bibcode: 1989MNRAS.238..729F

Fabian, A. C. & Vaughan, S. 2003, Monthly Notices of the Royal Astronomical Society, 340, L28, aDS Bibcode: 2003MNRAS.340L..28F

Ferrarese, L. & Merritt, D. 2000, The Astrophysical Journal, 539, L9, publisher: IOP Publishing

Fukumura, K., Kazanas, D., & Stephenson, G. 2009, The Astrophysical Journal, 695, 1199, aDS Bibcode: 2009ApJ...695.1199F

Gallo, L. C., Fabian, A. C., Grupe, D., et al. 2013, Monthly Notices of the Royal Astronomical Society, 428, 1191, aDS Bibcode: 2013MNRAS.428.1191G

Gallo, L. C., Miniutti, G., Miller, J. M., et al. 2011, Monthly Notices of the Royal Astronomical Society, 411, 607, aDS Bibcode: 2011MNRAS.411..607G

Gallo, L. C., Wilkins, D. R., Bonson, K., et al. 2015, Monthly Notices of the Royal Astronomical Society, 446, 633

García, J., Dauser, T., Lohfink, A., et al. 2014, The Astrophysical Journal, 782, 76, publisher: American Astronomical Society

García, J., Dauser, T., Reynolds, C. S., et al. 2013, The Astrophysical Journal, 768, 146, publisher: American Astronomical Society

George, I. M. & Fabian, A. C. 1991, Monthly Notices of the Royal Astronomical Society, 249, 352, aDS Bibcode: 1991MNRAS.249..352G

Grier, C. J., Peterson, B. M., Pogge, R. W., et al. 2012, The Astrophysical Journal, 744, L4, aDS Bibcode: 2012ApJ...744L...4G

Grupe, D., Komossa, S., & Gallo, L. C. 2007, The Astrophysical Journal, 668, L111, publisher: IOP Publishing

Grupe, D., Komossa, S., Gallo, L. C., et al. 2008, The Astrophysical Journal, 681, 982, publisher: IOP Publishing

Haardt, F. & Maraschi, L. 1991, The Astrophysical Journal, 380, L51

Houck, J. C. & Denicola, L. A. 2000, 216, 591, conference Name: Astronomical Data Analysis Software and Systems IX ADS Bibcode: 2000ASPC..216..591H

Jaroszynski, M. 1997, Acta Astronomica, 47, 399, aDS Bibcode: 1997AcA....47..399J

Kallman, T. 1999, Astrophysics Source Code Library, ascl:9910.008, aDS Bibcode: 1999ascl.soft10008K

Kerr, R. P. 1963, Physical Review Letters, 11, 237, publisher: American Physical Society

Laor, A. 1991, The Astrophysical Journal, 376, 90, aDS Bibcode: 1991ApJ...376...90L

Lense, J. & Thirring, H. 1918, Physikalische Zeitschrift, 19, 156, aDS Bibcode: 1918PhyZ...19..156L

Licklederer, S. 2019, PhD thesis

Martocchia, A., Matt, G., & Karas, V. 2002, Astronomy & Astrophysics, 383, L23, number: 3 Publisher: EDP Sciences

Miniutti, G. & Fabian, A. C. 2004, Monthly Notices of the Royal Astronomical Society, 349, 1435, aDS Bibcode: 2004MNRAS.349.1435M

Bibliography

Miniutti, G., Fabian, A. C., Goyder, R., & Lasenby, A. N. 2003, Monthly Notices of the Royal Astronomical Society, 344, L22, aDS Bibcode: 2003MNRAS.344L..22M

Mirabel, I. F. 2017, New Astronomy Reviews, 78, 1, arXiv: 1609.08411

Misner, C. 1973, Misner Thorne Wheeler - Gravitation (Freeman, 1973)

Moriyama, K., Mineshige, S., Honma, M., & Akiyama, K. 2019, The Astrophysical Journal, 887, 227, arXiv: 1910.10713

Pugliese, D. & Stuchlík, Z. 2015, The Astrophysical Journal Supplement Series, 221, 25, aDS Bibcode: 2015ApJS..221...25P

Rees, M. J. 1984, Annual Review of Astronomy and Astrophysics, 22, 471

Riaz, S., Ayzenberg, D., Bambi, C., & Nampalliwar, S. 2020, Monthly Notices of the Royal Astronomical Society, 491, 417

Richards, G. T., Strauss, M. A., Fan, X., et al. 2006, The Astronomical Journal, 131, 2766, aDS Bibcode: 2006AJ....131.2766R

Ross, R. R. & Fabian, A. C. 2005, Monthly Notices of the Royal Astronomical Society, 358, 211, aDS Bibcode: 2005MNRAS.358..211R

Shakura, N. I. 1973, Soviet Astronomy, 16, 756, aDS Bibcode: 1973SvA....16..756S

Shakura, N. I. 1987, Soviet Astronomy Letters, 13, 99, aDS Bibcode: 1987SvAL...13...99S

Shakura, N. I. & Sunyaev, R. A. 1973, Symposium - International Astronomical Union, 55, 155, publisher: Cambridge University Press

Shemmer, O., Netzer, H., Maiolino, R., et al. 2004, The Astrophysical Journal, 614, 547, aDS Bibcode: 2004ApJ...614..547S

Speith, R., Riffert, H., & Ruder, H. 1995, Computer Physics Communications, 88, 109

Steiner, J., McClintock, J. E., Narayan, R., & Gou, L. 2011, Black-hole spin measurement via X-ray continuum spectroscopy, conference Name: Fast X-ray Timing and Spectroscopy at Extreme Count Rates (HTRS 2011) Pages: 19 ADS Bibcode: 2011fxts.confE..19S

Thorne, K. S. 1974, The Astrophysical Journal, 191, 507, aDS Bibcode: 1974ApJ...191..507T

Vaughan, S. & Fabian, A. C. 2004, Monthly Notices of the Royal Astronomical Society, 348, 1415

Webster, B. L. & Murdin, P. 1972, Nature, 235, 37, aDS Bibcode: 1972Natur.235...37W

Wilkins, D. & Gallo, L. C. 2015, 225, 305.01, conference Name: American Astronomical Society Meeting Abstracts #225

Wilkins, D. R. & Fabian, A. C. 2011, Monthly Notices of the Royal Astronomical Society, 414, 1269, aDS Bibcode: 2011MNRAS.414.1269W

Wilkins, D. R. & Fabian, A. C. 2012, Monthly Notices of the Royal Astronomical Society, 424, 1284

Wilkins, D. R., Gallo, L. C., Grupe, D., et al. 2015, Monthly Notices of the Royal Astronomical Society, 454, 4440

Wilms, J., Reynolds, C. S., Begelman, M. C., et al. 2001, Monthly Notices of the Royal Astronomical Society, 328, L27, aDS Bibcode: 2001MNRAS.328L..27W

Yang, X. & Wang, J. 2013, The Astrophysical Journal Supplement Series, 207, 6

Eigenständigkeitserklärung

Ich versichere hiermit, die von mir vorgelegte Arbeit selbstständig verfasst zu haben. Alle Stellen, die dem Wortlaut oder dem Sinn nach aus veröffentlichten oder unveröffentlichten Werken anderer entnommen sind, wurden als solche gekennzeichnet. Sämtliche für die Anfertigung der Arbeit genutzten Quellen und Hilfsmittel sind angegeben. Diese Arbeit hat mit gleichem Inhalt bzw. in wesentlichen Teilen noch keiner anderen Prüfungsbehörde vorgelegen.

Erlangen, 23. August 2021,

....
(Jacob Rose)